Journal Pre-proof
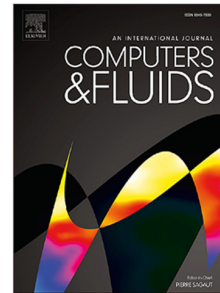
Study of the spatial transition in a plane channel flow

William I. Machaca Abregu, Enzo A. Dari, Federico E. Teruel

Please cite this article as: W.I. Machaca Abregu, E.A. Dari and F.E. Teruel, Study of the spatial transition in a plane channel flow. *Computers and Fluids* (2022), doi: https://doi.org/10.1016/j.compfluid.2022.105650.

STUDY OF THE SPATIAL TRANSITION IN A PLANE CHANNEL FLOW

William I. Machaca Abregu[a, b]**, Enzo A. Dari**[a, b, c] **and Federico E. Teruel**[a, b, c]

[a]*Departamento de Mecánica Computacional, Centro Atómico Bariloche, CNEA, Bariloche, Argentina,*
william.machaca@ib.edu.ar, http://mecom.cnea.gov.ar/

[b]*Instituto Balseiro, Centro Atómico Bariloche, CNEA-UNCUYO, Bariloche, Argentina*

[c]*CONICET, Centro Atómico Bariloche, CNEA, Bariloche, Argentina*

Abstract.

This study presents DNS results of the laminar-turbulent spatial transition in a plane channel flow. The transition is achieved imposing at the inlet the most unstable modes of the associated Orr-Sommerfeld and Squire eigenvalue problems. First, a study of the dependence of the transition on the intensity of the perturbations is presented. For $Re = 5000$, eleven simulations employing different amplitudes of the Tollmien-Schlichting and oblique waves were analyzed to find that the variation of the friction Reynolds number and shape factor downstream the departure of the transition is roughly independent on the amplitude of the perturbations and that the location of the peak in the friction Reynolds number is strongly dependent on the amplitude of each wave. This implies that, for the type of perturbations simulated here, the transitional phenomenon is essentially delayed or accelerated by the amplitude of the perturbations. Second, two cases with well different amplitude of perturbations are compared in detail. Results show that in both cases the following stages can be identified: quasi-linear stage, late stage, *spike* stage, peak transitional zone, post-transitional zone and fully turbulent zone. Moreover, downstream

the first state of the *spike* stage, both cases are essentially equal despite the fact that both transitions are separated by 50 channel half-height diameters in the streamwise coordinate. Finally, the physical phenomenon of the peak zone in the friction Reynolds number is explained considering the coherent vortices packet found across the height of the channel in the super-late stage of the transition.

1 INTRODUCTION

The understanding of the laminar-turbulent transition in a fluid flow is required in different engineering applications. In particular, this work is motivated by the study of transition in rectangular cooling channels with large aspect ratios. This geometrical characteristic allows modeling these devices employing a periodic boundary condition in the spanwise direction (channel width to channel height ratio, $W/H > 7$, (Vinuesa et al., 2014)). These types of channels are found in the fuel elements of nuclear research reactors ($W/H = 22$). Although modern research reactor operates within the turbulent regime (Teruel and Rizwan-uddin, 2009), the Argentinean research reactor RA6 may operate in a transitional regime since its last upgrade in power (Silin et al., 2010). Therefore, thermo-hydraulic and safety of this reactor is remarkably sensitive to flow conditions due to the strong variation of the friction and heat transfer coefficients in the transitional regime (Minkowycz et al., 2009; Abraham et al., 2010, 2011). For transitional flows, there are correlations based on experiments that can accurately predict, for instance, the pressure loss in channels as those studied here (see for example Gioia and Chakraborty (2006)). However, there is no organized data in the open literature to characterize the value of the friction coefficient in the spatial transition from the laminar regime to the fully turbulent one for different inflow conditions and Reynolds numbers. The variation of this parameter has been partially discussed in the following references Schlatter et al. (2006); Buffat et al. (2014).

More generally, the transition from laminar to turbulent flow is still nowadays a problem not fully understood even for flows in simple geometries such as pipes or rectangular channels (Sano and Tamai, 2016; Lorenzini and Salvigni, 2010; Benhamou and Galanis, 2004). These simple geometries have been extensively employed to study temporal and spatial transitions. On the experimental side, results are very costly to obtain, as the proliferation of turbulence requires capturing the spatial scale of the spreading and decay of the process while structures are moving downstream at the average mean velocity. For instance, in the experiment of Avila et al. (2011), a length of 3750 pipe diameters is employed. A relatively modest length of 440 channel diameters is employed in Lemoult et al. (2014). In these experiments, the evolution of turbulent spots in a transitional channel is studied resembling the pioneering study of instability in the

boundary layer flow by Klebanoff et al. (1962). Numerical simulations have been extensively employed to study the space-time evolution of disturbances in transitional flows. Likely due to the computational cost involved, temporal transitions, that employ periodic domains in two spatial directions, are more easily found and have been successful in predicting experimental observations (Kleiser and Zang, 1991). Some relevant DNS studies in the temporal transition in a plane Poiseuille flow are: Zang and Krist (1989); Henningson et al. (1993); He and Seddighi (2013); Luo and Hui (2004). These studies exemplified the capabilities of the numerical simulation as a powerful tool to study the physics of the transition. The simulation of the spatial transition, although more computationally intensive, offers a direct comparison with experimental observations. One of the techniques employed to simulate the spatial transition is to perturb the inflow conditions with the two-dimensional (primary) disturbances, also known as the Tollmien-Schlichting waves (T-S), that become susceptible to three- dimensional disturbances at some finite amplitude (i.e. oblique waves). The study of Lundbladh et al. (1994) and Liu and Liu (1995) show the complete transitional scenario employing this type of perturbations obtained from the solution of the Orr-Sommerfeld and Squire equations. The study of Saiki et al. (1993) employs a similar technique to simulate the H- and K-type transitions in the plane Poiseuille flow. Similarly, but employing LES, the transition has also been successfully simulated in Schlatter et al. (2006). In this study, a comparison between the temporal and spatial transition is carried out trying to determine a correspondence between time and space in both transitional scenarios.

While the linear and early weakly non-linear stages of transitional flow are relatively well understood (Chen and Liu, 2011; Lu and Liu, 2012), the late and super-late non-linear transitional stages still have questions to answer. We will discuss here the physics involved in the friction Reynolds number or friction factor's peak (super-late stage) that characterizes the transitional process at moderate Reynolds numbers (Machaca Abregu and Teruel, 2016) analyzing the three-dimensional vortices structures: the Λ, *hairpin* and *ring* vortices. On this regard, it has been shown that in the K-type transition, the TS wave interacts with oblique waves to yield a Λ vortex. As the flow develops, the Λ vortex generates at its tip a ring-type vortex. The ring vortex

with two quasi-streamwise vortices is known in the literature, after Theodorsen (Theodorsen, 1952), as a *hairpin* vortex and is composed by three parts: head, neck and two legs (Adrian et al., 2000; Wang et al., 2016). These vortices yield downward jets (sweep), which bring high energy from the bulk of the flow towards the wall, and upward jets (ejection), which bring low velocity flow from the wall towards the bulk (Borodulin et al., 2002a; Guo et al., 2010). Both mechanisms mix the flow yielding large shear layers that result in an increase of the friction factor.

Moreover, different types of sweep-ejection mechanisms can be identified according to the formative state of the *hairpin* vortex. When the Λ vortex or the legs of the *hairpin* vortex are present, the first sweep and first ejection are produced. This mechanism was identified numerically and experimentally by Borodulin et al. (2002a) and Liu and Chen (2010). When the ring vortex is present, there is a second sweep and second ejection mechanism with higher intensity than the former (Chen and Liu, 2011; Guo et al., 2010). A scheme of these mechanisms is shown in Figure 1. The principal characteristic of the *ring* vortex is that near the neck of the *hairpin* vortex the mechanism yields high shear layer areas that are unstable and yield small scales structures (Lu et al., 2012a) (i.e.small scales structures are generated by multilevel positive spike instead of large vortex breakdown (Lu and Liu, 2012)). The increase of the intensity of these spikes, and thus the generations of shear layer areas, continues until the ring vortex ceases to be perpendicular to the flow direction (Lu and Liu, 2012). After this stage, the vortex deforms and dissipates and thus it reduces the production of small-scales structures. However, in the process of the formation and evolution of the hairpin vortex, chains ring vortices are generated upstream the leading vortex as a consequence of the Helmholtz vorticity conservation law (Lu et al., 2012b; Zhou et al., 1999; Wang et al., 2016). These ring vortices appear one by one (Lu et al., 2012b) and are called a coherent packet (Zhou et al., 1996, 1999). When the intensity of the downward jet decreases in the primary hairpin vortex (due to its change in slope and deformation), the upstream vortices begin to grow and to be perpendicular to the flow direction causing the growth of the shear stress. This is the main reason that explains the existence of a high shear layer upstream of the leading *ring* vortex. Using this description of the flow, we

will discuss the peak zone (super-late stage) in the spatial transitional channel flow.
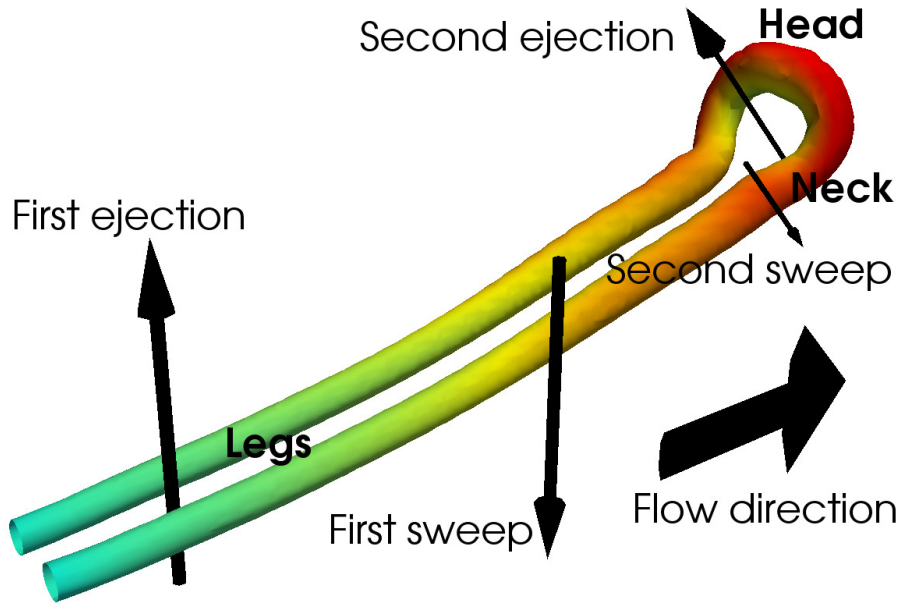

Figure 1: *Hairpin* vortex in spatial laminar-turbulent transitional channel flow simulated by Machaca Abregu and Teruel (2016).

In the present contribution, DNS is carried out to simulate the spatial transition to achieve different goals. In the first part of this study, the numerical method is presented. The inflow and outflow boundary conditions are described and validated. Next, a grid independence study is employed to determine an accurate and cost-effective production grid. Next, a useful parameter for engineering calculations, the friction Reynolds number (or equivalently, the friction factor), is computed for different amplitude of the perturbations imposed at the inlet. Later, a comparison between two simulations with very different amplitude of perturbations is carried out to evaluate the effect of the perturbation in the late stage and super-late stage of the transition. Finally, the physical phenomenon of the friction factor's peak in the transitional zone is discussed using the actual knowledge of the *hairpin* vortex growth and sweep-ejection mechanism in transitional flows. Conclusions are finally drawn in the last section.

2 NUMERICAL METHOD

The finite difference code Incompact3d (Laizet and Lamballais, 2009; Laizet et al., 2010; Laizet and Li, 2011) is used to solve the incompressible and dimensionless Navier-Stokes equa-

tions, written in cartesian coordinates as:

$$\frac{\partial \vec{u}}{\partial t} + \frac{1}{2}(\nabla(\vec{u} \otimes \vec{u}) + (\vec{u} \cdot \nabla)\vec{u}) = -\nabla p + \frac{1}{Re}\nabla^2 \vec{u}, \tag{1}$$

$$\nabla \cdot \vec{u} = 0, \tag{2}$$

where the distance $\vec{x}$, instantaneos velocity $\vec{u}$, pressure p and time t are dimensioned with the channel half-height h, the maximum velocity in the streamwise direction U_o, the constant density ρ and the constant kinematic viscosity ν. Therefore, Re is the Reynolds number based on U_o and h. The convective term is written as it is numerically treated, in the skew-symmetric form, to enable the reduction of aliasing errors and improvement of kinetic energy conservation for the spatial discretization used in the code. For the spatial differentiation, sixth-order centered compact schemes are used. The time integration is performed using a second-order Adams-Bashforth scheme with an approximated time step of 10^{-3} due to the CFL restriction. The simulated domain is a parallel channel flow (Figure 2) with the x-coordinate chosen as the streamwise direction. No-slip boundary conditions are ensured in a conventional way at the top and bottom of the computational domain ($y = 0, 2$) imposing a Dirichlet condition on the velocity. In the spanwise direction (z), periodicity is assumed. Inlet and outlet boundary conditions are not straightforward and are described below. For more information about the code Incompact3d (numerical method and parallelization strategy) visit http://www.incompact3d.com/.

For most calculations, the computational domain $L_x \times L_y \times L_z = 90 \times 2 \times 3$ was discretized on a cartesian grid (slightly stretched in the y-direction) of $n_x \times n_y \times n_z = 1800 \times 65 \times 64$ points. This grid will be called the production grid in the rest of the study. For fully developed conditions and $Re_\tau \approx 210$ the near-wall resolution of the production grid is given in plus unit by $x^+ = 11$, $y^+ = 2$ and $z^+ = 10$. This resolution was found cost-effective for the purposes of the study. Additionally, other resolutions were employed to verify the independence of results on the production grid. The longest computation run required approximately ten wall days with the available computational resources.
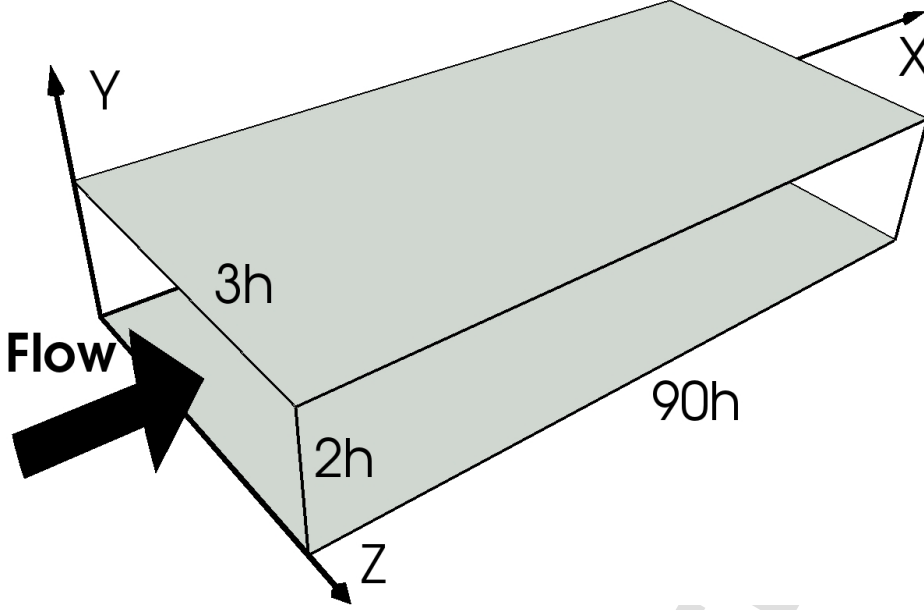
Figure 2: Computational domain.

2.1 Inlet Boundary Conditions

In comparison with the simulation of the temporal transition, the spatial transition is computationally expensive (Herbert, 1988). The domain simulated must be long enough in the streamwise direction to allow the flow to transition from the laminar state to a fully developed turbulent one. Therefore, the mechanism to trigger the transitional process must be effective enough to reduce the portion of the domain with the laminar regime. Possibly, the most effective way to trigger the transitional process is to perturb the flow with the most unstable modes of the Orr-Sommerfeld and Squire eigenvalue problem. This methodology has been successfully employed for the boundary layer problem as well as for the parallel channel flow (Lundbladh et al., 1994). For a base flow depending only on the y-coordinate (i.e. the laminar solution or Poiseuille flow for the present domain) and for perturbations at the inlet for the wall-normal velocity ($\tilde{v}$) and wall-normal vorticity ($\tilde{\eta}$) of the form:

$$\tilde{v}(x, y, z, t) = \hat{v}(y)e^{i(\alpha x + \beta z - \omega t)}, \tag{3}$$

$$\tilde{\eta}(x, y, z, t) = \hat{\eta}(y)e^{i(\alpha x + \beta z - \omega t)}, \tag{4}$$

the Orr-Sommerfeld and Squire equations reduce to the following eigenvalue problem:

$$[(-i\omega + i\alpha U)(D^2 - \alpha^2 - \beta^2) - i\alpha U'' - \frac{1}{Re}(D^2 - \alpha^2 - \beta^2)^2]\hat{v} = 0, \tag{5}$$

$$[(-i\omega + i\alpha U) - \frac{1}{Re}(D^2 - \alpha^2 - \beta^2)^2]\hat{\eta} = -i\beta U'\hat{v}, \tag{6}$$

where D stands for the differential operator in the wall-normal direction and $'$ stands for the derivative in the same direction. These equations can be solved prescribing the boundary conditions $\hat{v} = D\hat{v} = \hat{\eta} = 0$ at the walls for the plane channel flow or at the free stream for the boundary layer. For the spatial problem, the eigenvalue α is obtained following a strategy shortly reviewed here (Lundbladh et al., 1994). First, the 4th-order problem is reduced to a 2nd-order one by the transformation:

$$\begin{pmatrix} \hat{v} \\ \hat{\eta} \end{pmatrix} = \begin{pmatrix} \hat{V} \\ \hat{E} \end{pmatrix} exp(-\alpha y), \tag{7}$$

Then, the non linear problem can be linearized employing an additional variable, $\alpha\tilde{V}$. The final linear eigenvalue problem results in:

$$\begin{pmatrix} -R_1 & -R_0 & 0 \\ I & 0 & 0 \\ 0 & -S & -T_0 \end{pmatrix}\begin{pmatrix} \alpha\hat{V} \\ \hat{V} \\ \hat{E} \end{pmatrix} = \alpha\begin{pmatrix} R_2 & 0 & 0 \\ 0 & I & 0 \\ 0 & 0 & T_1 \end{pmatrix}\begin{pmatrix} \alpha\hat{V} \\ \hat{V} \\ \hat{E} \end{pmatrix}, \tag{8}$$

with

$$R_2 = \frac{4}{Re}D^2 + 2iUD, \tag{9}$$

$$R_1 = -2i\omega D - \frac{4}{Re}D^3 + \frac{4}{Re}\beta^2 D - iUD^2 + iU\beta^2 + iU'', \tag{10}$$

$$R_0 = i\omega D^2 - i\beta^2 D^2 + \frac{1}{Re}D^4 - \frac{2}{Re}\beta^2 D^2 - iUD^2 + \frac{1}{Re}\beta^4, \tag{11}$$

$$T_1 = \frac{2}{Re}D + iU, \tag{12}$$

$$T_0 = -i\omega - \frac{1}{Re}D^2 + \frac{1}{Re}\beta^2, \tag{13}$$

$$S = i\beta U^{'}. \tag{14}$$

We employ the open-source language Octave to develop a code to solve the eigenvalue problem given in Eq. (8). This code is based on an available one developed to calculate the temporal eigenvalue problem (Juniper, 2014; Schmid and Henningson, 2001). It employs the Chebyshev collocation method to carry out the derivatives required by the differential operators. The imposition of the boundary conditions on these operators is carried out following the technique given in Trefethen (2000). The code has been extensively validated. A brief resume of this validation is presented here comparing our results with data extracted from the open literature. It is worth noting however that although rich data can be found to test parameters calculated for the temporal eigenvalue problem, only a few cases are available to test the solution of the spatial one. First, the eigenvalue spectrum is evaluated. For the parameters given in Table 1, the spatial eigenvalue α is very well compared with values obtained by Saiki et al. (1993) (Table 2). Additionally, the most unstable eigenvalues obtained in Schmid and Henningson (2001) for $Re = 2000$, $w = 3$ and $\beta = 0$ does not show differences with those calculated in this study (Table 3). The complete spectrum is also very well compared with available data in Machaca Abregu (2015).

Caso	Re	ω_{2d}	ω_{3d}	β
I	5000	0.33698	0.33698	1
II	5000	0.33698	0.16849	1
III	5000	0.33698	0.33698	2
IV	5000	0.33698	0.16849	2

Table 1: Parameters employed by Saiki et al. (1993) to solve the spatial eigenvalue problem.

.

The eigenfunctions are difficult to validate. To the knowledge of the authors, there is only

Caso	α_{2dR}	α_{2dC}	α_{3dR}	α_{3dC}
I	1.17249+0.012873i	1.1724**7**+0.0128**02**i	1.02570+0.068456i	1.025**68**+0.06845**0**i
II	1.17249+0.012873i	1.1724**7**+0.0128**02**i	0.52293+0.019645i	0.5229**2**+0.01967**6**i
III	1.17249+0.012873i	1.1724**7**+0.0128**02**i	0.91984+0.258357i	0.9198**3**+0.25836**0**i
IV	1.17249+0.012873i	1.1724**7**+0.0128**02**i	0.37243+0.083078i	0.37243+0.08**0377**i

Table 2: Eigenvalues calculated for the Orr-Sommerfeld problem and parameters given in Table 1. α_{2dR} and α_{3dR} are given in Saiki et al. (1993), and α_{2dC} and α_{3dC} are calculated in the present study. Bold numbers emphasize the difference.

α_{2dR}	α_{2dC}
0.97875+0.044394i	0.97875+0.044394i
0.61167+0.140492i	0.61167+0.14049i
0.34312+0.049677i	0.34312+0.049677i

Table 3: Eigenvalues calculated for the Orr-Sommerfeld problem and Re = 2000, ω = 0.3 and β = 0. α_{2dR} are given by Schmid and Henningson (2001); and α_{2dC} are computed in the present study.

available data in Schlatter (2005). This reference reports the eigenvalue spectrum for Re = 5000 and ω = 0.3, for the bi-dimensional case (β = 0) and for the three-dimensional case (β = 2.0944). The most unstable eigenvalues ($2D$ and $3D$ cases) obtained in Schlatter (2005) are not exactly equal to those calculated here (for Schlatter (2005) $\alpha = 1.08 + 4.44 \times 10^{-3}i$ and $\alpha = 0.803 + 0.231i$ while for the present study $\alpha = 1.08 + 4.60 \times 10^{-3}i$ and $\alpha = 0.787 + 0.223i$, respectively). Nevertheless, the eigenfunctions reported for the most unstable eigenvalues in Schlatter (2005) are in excellent agreement with present results (see Figure 3). This short validation gives enough support to claim that the spatial eigenvalue problem is correctly solved.
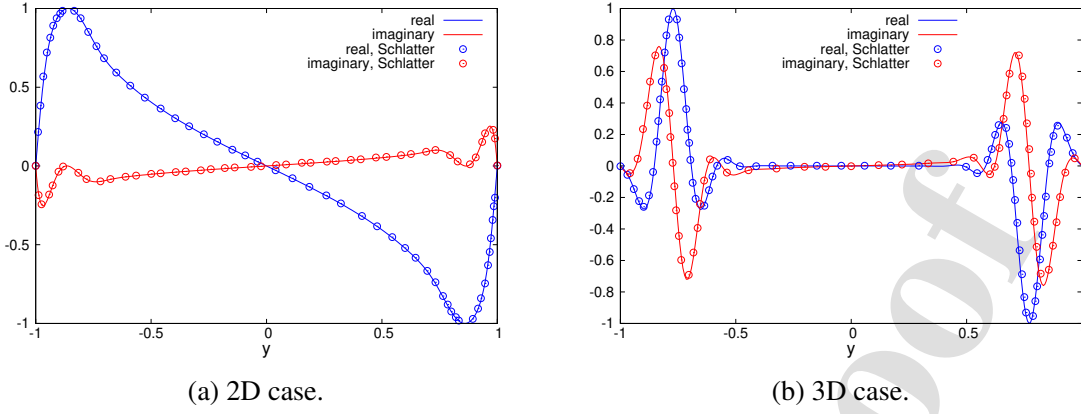
Figure 3: Comparisson of streamwise eigenfunctions between present results (lines) and Schlatter (2005) results (symbols). Blue lines correspond to the real part and red lines to the imaginary part. 2D case for $Re = 5000$, $\omega = 0.3$ and $\beta = 0$. 3D case for $Re = 5000$, $\omega = 0.3$ and $\beta = 2.0944$.

With the solution of the Orr-Sommerfeld and Squire equations at hand, the inflow boundary condition is prescribed as:

$$\vec{U} + \vec{\tilde{u}}, \tag{15}$$

where $\vec{U} = (U(y), 0, 0)$ is the Poiseuille base flow and $\vec{\tilde{u}} = (\tilde{u}, \tilde{v}, \tilde{w})$ is the perturbation given by:

$$\begin{aligned}
\vec{\tilde{u}}(x = 0, y, z, t) &= A_{2d}\mathbb{R}[(\vec{\tilde{u}}_{2d}(y))e^{-i\omega_{r2d}t}] \\
&+ \frac{1}{2}A_{3d}\mathbb{R}[(\vec{\tilde{u}}_{r3d}^{+}(y))e^{i(\beta z - \omega_{r3d}t)}] + \frac{1}{2}A_{3d}\mathbb{R}[(\vec{\tilde{u}}_{r3d}^{-}(y))e^{i(\beta z - \omega_{r3d}t)}]
\end{aligned} \tag{16}$$

where A_{2d} and A_{3d} are the amplitude of the bi-dimensional (T-S waves) and oblique waves respectively. The complex eigenfunctions, $\vec{\tilde{u}}_{2d}$ and $\vec{\tilde{u}}_{3d}$, are calculated solving the Orr-Sommerfeld and Squire problem for a given Re, wave number in the z-direction (β), and the angular frequency in two and three dimensions, ω_{2d} y ω_{3d}, respectively. In this study the eigenfunctions have been normalized so that the maximum amplitude of their streamwise component is one for a zero phase-shift. The upper indexes $+$ and $-$ correspond to the eigenfunctions calculated for $\beta > 0$ and $\beta < 0$, respectively. It is well known that perturbations with $\omega_{r3d} = \omega_{r2d}$ yield K-type instabilities and the case with $\omega_{r3d} = \frac{1}{2}\omega_{r2d}$ corresponds to H-type instabilities (Saiki et al., 1993). The implementation of the inflow boundary condition in incompact3D is straight-

forward as the inlet velocity needs to be prescribed at each time-step when the inflow-outflow boundary condition is employed.

2.2 Outlet Boundary conditions

For non periodic turbulent flows, the outlet boundary condition is an issue that needs to be specifically addressed for each numerical implementation. Ideally, this condition needs to be capable to avoid spurious reflections of waves at the outlet that can weaken the stability of the numerical computation. One way to sort out this problem is the fringe method. This method allows to employ periodic boundary conditions in the stream-wise direction by relaminarizing the flow near the outlet (Schlatter et al., 2006; Buffat et al., 2014). Other option is to employ a buffer domain. In this case, the buffer domain is added at the outlet of the physical domain where the governing equations are modified reducing the streamwise viscous term (Criminale et al., 1997). In these two methodologies, approximately 20% of the computational domain is dedicated to impose the outflow boundary condition. The code Incompact3D allows to impose a relatively simple convective boundary conditions at the outlet. Therefore, the first step was to evaluate the response of the code to the use of this boundary condition for our simulations.

To prescribe the velocity at the outlet, a standard convective boundary condition is solved in Incompact3D:

$$\frac{\partial \vec{u}}{\partial t} + U_c \frac{\partial \vec{u}}{\partial x} = 0, \tag{17}$$

where U_c is, in general, a constant convective average velocity. The study of Lamballais (2014) for a rotating parallel channel flow with an expansion gives a useful insight on this regard. Lamballais (2014) found that when a constant average velocity is used as the convective velocity, the numerical solution is not always stable. Nevertheless, when the Poiseuille laminar profile is used as convective velocity:

$$U_c(y) = y(2 - y), \tag{18}$$

the time evolution of the initial condition is very robust introducing only moderate spurious effect in the near-outlet region. In our simulations this test was repeated with similar results. The use of a constant average velocity as convective velocity yields spurious oscillations that

grow in the near outlet region up to a point where the numerical solution becomes unstable. This effect can be mitigated applying a very costly reduction of the time step. However, the use of the parabolic profile as convective velocity was found to be numerically very robust (i.e. the maximum time step that allows a stable numerical solution is approximately the same than that found for the same grid and parameters but with periodic boundary conditions in the streamwise direction). Although spurious effects are clearly observed in the near-outlet region of our simulations they are mainly limited to the region $x \geq L_x - 5$ (i.e. the last 5 channel half-heights).

To give a clear insight that spurious effects do not pollute the numerical solution outside the near-outlet region, we compared our statistics of the turbulent channel flow upstream of this region with a reference. We simulated the spatial transition for $Re = 4200$ with a spatial resolution and parameters that correspond to the production grid. Here, we are only interested in the quality of our fully developed turbulent solution downstream of the transition and upstream of the near-outlet region. First, the spurious effects are shown. Figure 4 shows the friction Reynolds number, a quantity proportional to square root of the friction coefficient (Quadrio et al., 2016), along the streamwise coordinate for the transition simulated (note that $Re_\tau = \frac{u_\tau h}{\nu}$, where u_τ is the friction velocity averaged in time and in the periodic coordinate). The near-outlet region has been zoomed in to indicate the spurious effects that show up as a sudden drop in the value of this parameter in the near outlet region. The quality of the solution upstream of the near outlet region is shown in Figure 5. Two turbulent statistics ($\sqrt{< u_i'^+ u_i'^+ >}$ and $\sqrt{< \omega_i'^+ \omega_i'^+ >}$, the root-mean-square (rms) of the turbulent fluctuating velocity components and the turbulent fluctuating vorticity components in wall units respectively) are considered. Three sets of data are displayed for comparison: the reference (Moser et al., 1999), results at the location $x = L_x - 5 = 85$ in Figure 4, and our results for a periodic box with the same spatial and temporal resolution than that employed in the spatial transitional case. The agreement is good enough to show that the numerical solution in the near-outlet region is not polluted by the imposition of the convective boundary condition. It is then concluded that the use of Eq. 17 employing Eq. 18 as convective velocity is robust, easy to implement in Incompact3d, and computationally

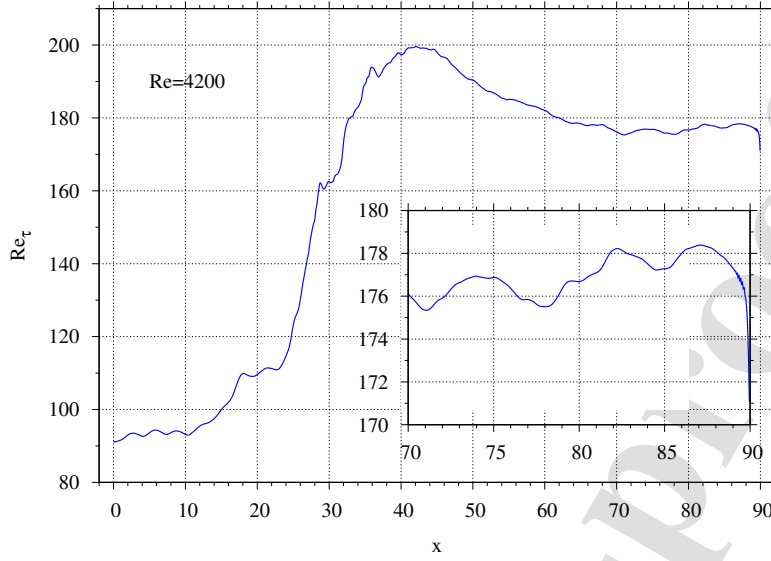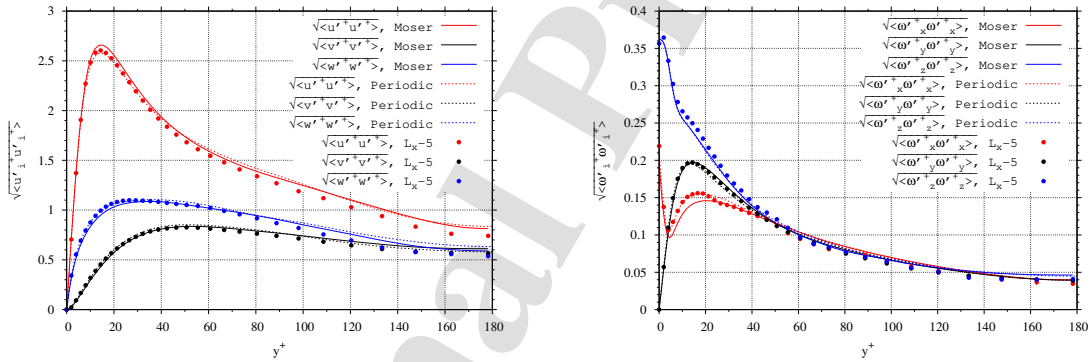cheaper than other methodologies employed in the literature.

Figure 4: Space evolution of Re_τ from laminar to turbulent (Re = 4200). Spurious effects are zoomed in.

(a) Rms of turbulent fluctuating velocities.

(b) Rms of turbulent fluctuating vorticities.

Figure 5: Fully developed turbulent statistics from Moser et al. (1999) , present results for a periodic box and for the spatial transition simulation at $x = 85$ (Figure 4). Re = 4200.

2.3 Grid dependence results

Present results show that the domain length in the streamwise direction must be at least 90 channel half-heights to capture the transition to a fully established turbulent regime. Therefore, the number of grid points in this direction could be a bottle neck. We define a production grid establishing two criteria to evaluate the quality of the results computed with this grid. The first one is to compare the fully developed flow upstream of the near outlet region ($x \approx L_x - 5$)

with available DNS data. The second one is to perform a single simulation in a finer grid that approximately doubled the number of grid points per direction than those used in the production grid. We will show that these two comparisons reveal that the production grid is sufficient for the purposes followed in this study.

Present numerical experiments allowed to determine that $\Delta x = 0.05$ is a value that yields a reasonable computational cost with good accuracy and stable numerical computations (Machaca Abregu, 2015) (equivalent to 1800 grid points in 90 channel half-heights). In the wall-normal direction, the grid refinement is mainly defined by a grid that yields a fully developed turbulent profile that is well compared with available DNS data. For present simulations, an averaged $\Delta y = 0.03$ is considered sufficient for the highest Reynolds numbers simulated (this corresponds to 65 elements in the wall-normal direction). Additionally, some computational savings can be obtained by considering carefully the wave-number of the perturbation imposed in the spanwise direction, β. At least, a period of the perturbation must be simulated, so larger values of β require shorter lengths in this direction. Following these considerations, we avoid the well studied case with $\beta = 1$ (Saiki et al., 1993) and we choose, instead, the case with $\beta = 2.0944$ (Schlatter, 2005). In addition, it is found that $\Delta z = 0.07$ is a value that yields good results to describe the fully turbulent regime in fully periodic simulations (Machaca Abregu, 2015). Alter all, $L_z = 3$ and $n_z = 64$ ($\Delta z = 0.05$) ensures a sufficient discretization in the spanwise direction.

The first criterion to evaluate the production grid is presented. For the highest Re number simulated in this study ($Re = 5000$), the production grid with $\Delta x = 0.05$, $\Delta y = 0.03$ (averaged value) and $\Delta z = 0.05$ is compared, in the fully developed region, with a fully periodic simulation that employs the same grid resolution than that used in the production grid. Figure 6 shows good agreement for the statistics of the fully developed turbulent channel flow (note that Incompact3D has already been validated for the turbulent channel flow (Laizet and Lamballais, 2009)). Additionally, the spatial evolution of Re_τ obtained with the production grid is compared with computations that vary computational parameters. First, Figure 7a shows results for $Re = 4200$ with one grid that doubles the resolution per direction used in the production grid, and other that keeps the spatial resolution fixed but doubles the number of time steps employed

to carry out statistics. Figure 7b shows the spatial transitions varying the spanwise width (L_z) for Re = 5000. The comparison shown in Figure 7 and Figure 6 suggests that the production grid is sufficient to compute the friction Reynolds number in the transitional scenarios proposed in this study and therefore it was employed to obtain results presented in the following sections.
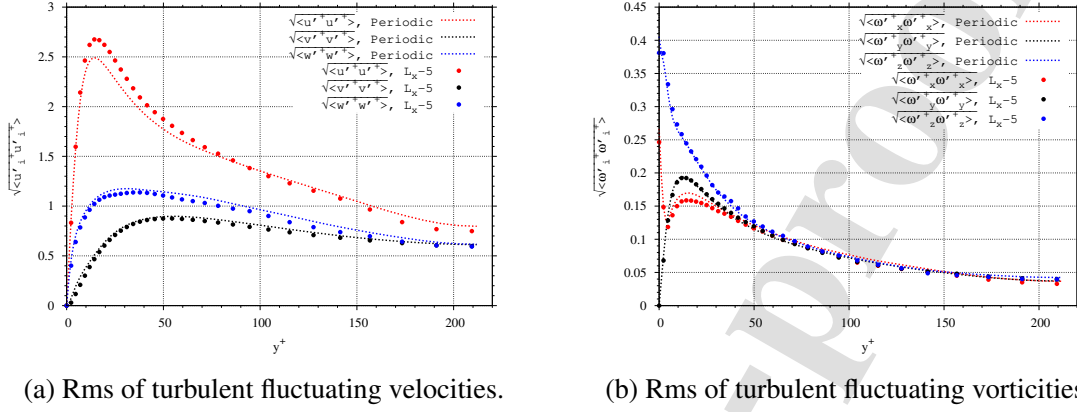

(a) Rms of turbulent fluctuating velocities.

(b) Rms of turbulent fluctuating vorticities.

Figure 6: Fully developed turbulent statistics for Re = 5000. Periodic box and spatial transition.

(a) Variation of the spatial resolution.
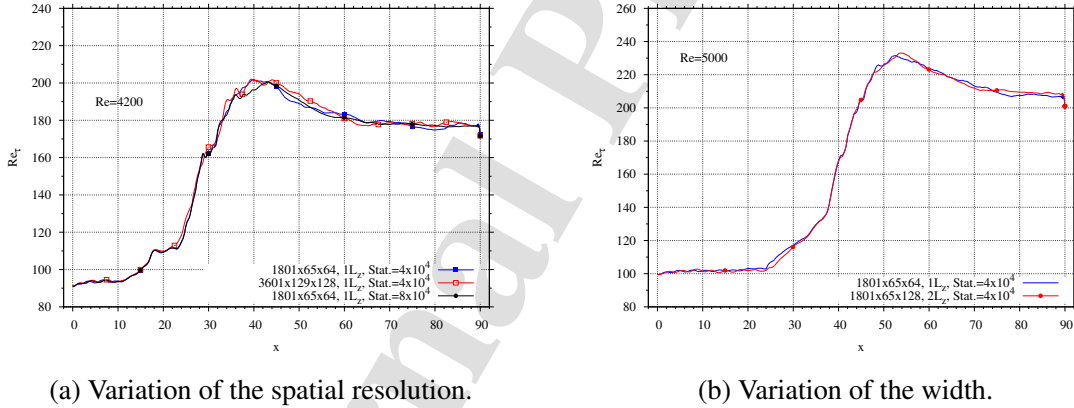

(b) Variation of the width.

Figure 7: Space evolution of Re_τ in the transition for different parameters of the simulation. The legend "Stat." refers to the number of time-points employed to carry out the time averaging.

3 RESULTS

3.1 Dependence of integral quantities on the amplitude of perturbations

We will discuss the speed of development of the transitional process with the amplitude of the perturbations imposed at the inlet analyzing results of Re_τ and shape factor (H) at Re = 5000. We have let fixed the parameters of the 2D and 3D waves imposed at the inlet (β = 2.0944,

w_{2d} = 0.3 and w_{3d} = 0.3) together with the eigenfunctions corresponding to the most unstable eigenvalue (Figure 3). A total of 11 simulations were carried out varying the amplitude of the 2D and 3D waves, A_{2d} and A_{3d} respectively. Table 4 shows simulated amplitudes and the corresponding inlet turbulent intensity Tu ($Tu = \sqrt{2/3k}$), where k is the turbulent kinetic energy ($k = \int_0^2 \frac{<u'u'>+<v'v'>+<w'w'>}{2} \partial y$, where $<>$ means averaged in time and z).

A_{2d}	A_{3d}	$Tu(\%)$
6	0.05	2.24
6	0.1	2.24
6	0.2	2.24
6	0.4	2.24
6	0.8	2.24
3	0.2	1.20
3.5	0.2	1.39
4	0.2	1.59
4.5	0.2	1.80
9	0.2	3.58
12	0.2	4.77

Table 4: Different inlet conditions simulated. Amplitude of the T-S and 3D oblique waves for Re = 5000 and the corresponding inlet turbulent intensity.

Figure 8 shows the streamwise evolution of the friction Reynolds number for cases described in Table 4 where Figure 8a and 8b are for fixed A_{2d} and A_{3d}, respectively (note that the case with A_{2d} = 3 does not achieve transition in the domain simulated). Additionally, a reference data calculated by Schlatter (2005) using the ADM-RT model is presented for comparison purposes (A_{2d} = 6% and A_{3d} = 0.2%). On the one hand, both figures clearly show that the increase of the amplitude of any of these two components accelerates the departure of the transition, changing, for instance, the location of the peak of the friction Reynolds number in approximately 33 channel half-heights (cases with A_{2d} = 3.5% and A_{2d} = 12% in Figure 8b respectively). On the other hand, the shape of the streamwise evolution of Re_τ, characterized by a fast growth, peak and decay to a fully turbulent value, is qualitatively similar for all transitions. Moreover, a quick review of Table 4 and Figure 8 reveals that cases characterized by almost the same inlet turbulent intensity result in locations of the departure of transition that differs in several channel half-heights. This shows that the value of Tu by itself is not enough to predict the location of

the onset of transition as it is usually hypothesized in RANS models (Minkowycz et al., 2009).
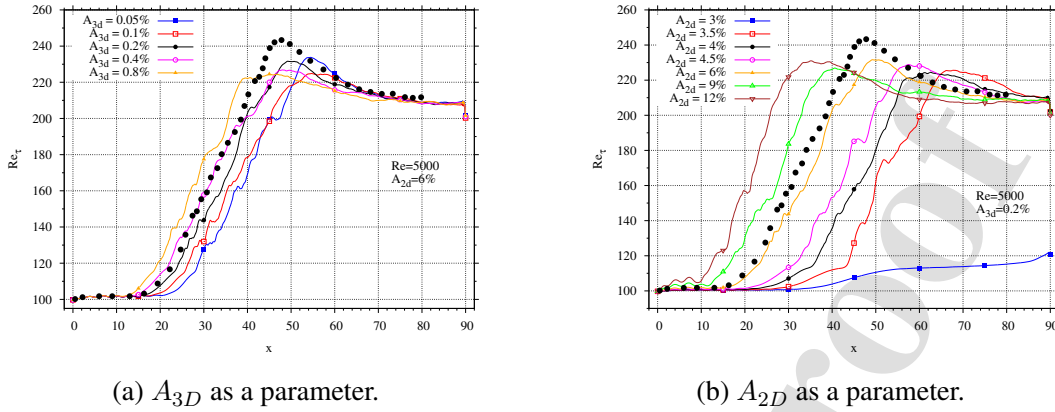
(a) A_{3D} as a parameter.

(b) A_{2D} as a parameter.

Figure 8: Space variation of Re_τ with the amplitude of the T-S and oblique waves as parameters ($Re = 5000$). The data calculated by Schlatter (2005) is shown in black dots.

These aspects suggest that the amplitudes of the perturbations delay or accelerate the transitional process but do not significantly affect the shape of integral quantities. Rather arbitrarily and following these ideas we choose the following criterion to define a methodology that allows to find similarities between the different transitional scenarios. The curves shown in Figure 8 are shifted so the maximum of each one coincides with each other (i.e. curves are shifted to the left so that the maximums are superimposed with the case that achieves a transition in the shortest distance from the inlet, $A_{2d} = 12\%$ and $A_{3d} = 0.2\%$). This shift, shown in Figure 9, allows to conclude that the variation of the friction Reynolds number from the onset of transition to the fully turbulent state is fairly independent on the amplitude of perturbations, at least for the range of parameters simulated here. An implication of this claim that can be used in RANS modeling is that a model that fits a particular transitional scenario may employ the intensity of perturbations to modify, only, the spatial location of its onset. Another aspect that can be inferred from Figure 9, directly related to engineering applications, is that the pressure drop during the transition (i.,e. from the onset to the fully turbulent state) is fairly independent on the intensity of the perturbations.
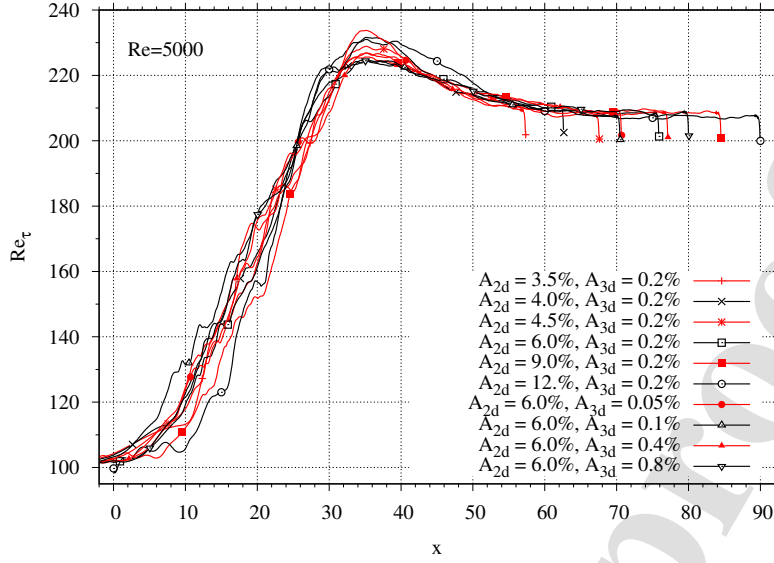
Figure 9: Space shifted Re_τ for cases described in Table 4.

The criterion chosen to shift the curves allows to explore the dependence of the peak location on the values of the amplitude. Figure 10 shows the non dimensional values of the distances shifted in the streamwise direction as a function of the amplitude of perturbations simulated. Two power laws are fitted, one for the case where A_{3d} is kept fixed and equal to 0.2% and the other one where A_{2d} is equal to 6%. These laws predict calculated values within a 10% of accuracy. As expected, the peak location exhibits a stronger sensitivity to A_{2d}, the amplitude of the primary instability (TS wave, with finite amplitude), than that shown to the secondary instability (a pair of oblique waves, with infinitesimal amplitude). That is, the location on the onset varies more for the same percentage change of the amplitude of the TS wave than that for the oblique waves. This behavior is expected because the TS waves are more unstable than the 3D oblique waves in the present linear stability analysis (see section 2.1).
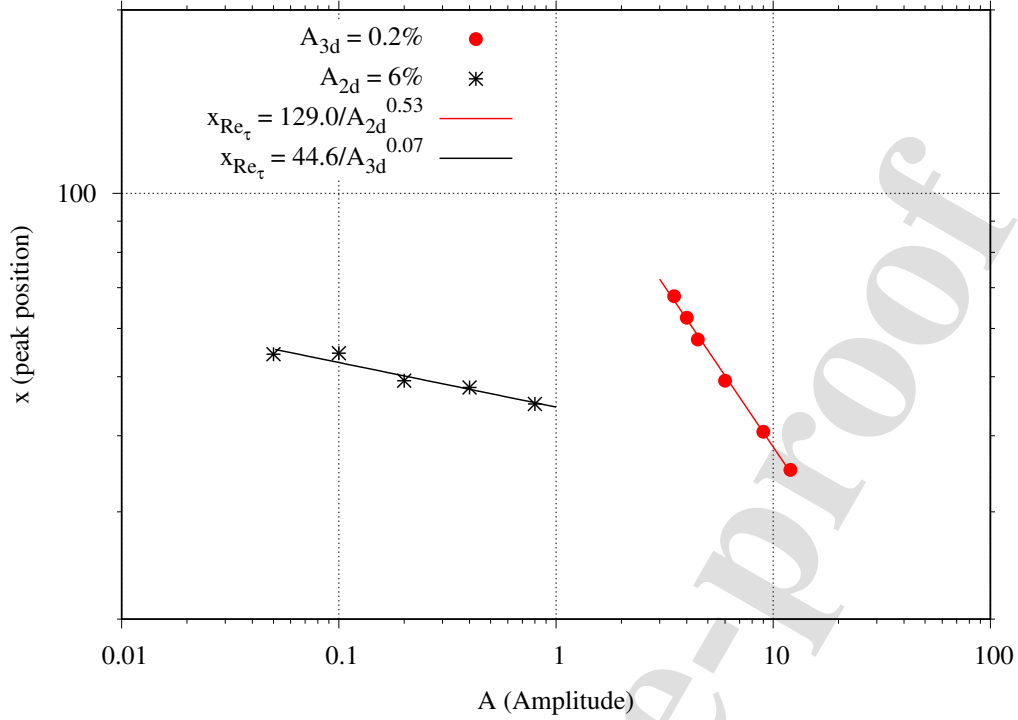
Figure 10: Space location of the Re_τ peak with the amplitude of the T-S and oblique waves ($Re = 5000$).

Other quantity of interest, the shape factor (H), is shown in Figure 11. Both, the calculated laminar and fully turbulent values of this quantity, 2.5 and 1.6 respectively, are in perfect agreement with the literature (Seki and Matsubara (2012), Schlatter et al. (2004)). The streamwise evolution is, also, in good agreement with results calculated by Schlatter (2005). As expected, based on previous results, the shape factor's evolution is more sensible to A_{2d} than A_{3d} and its shape is fairly independent on the amplitude of the perturbations as can be appreciated in Figure 11c, where the quantities have been shifted according to laws calculated in Figure 10.
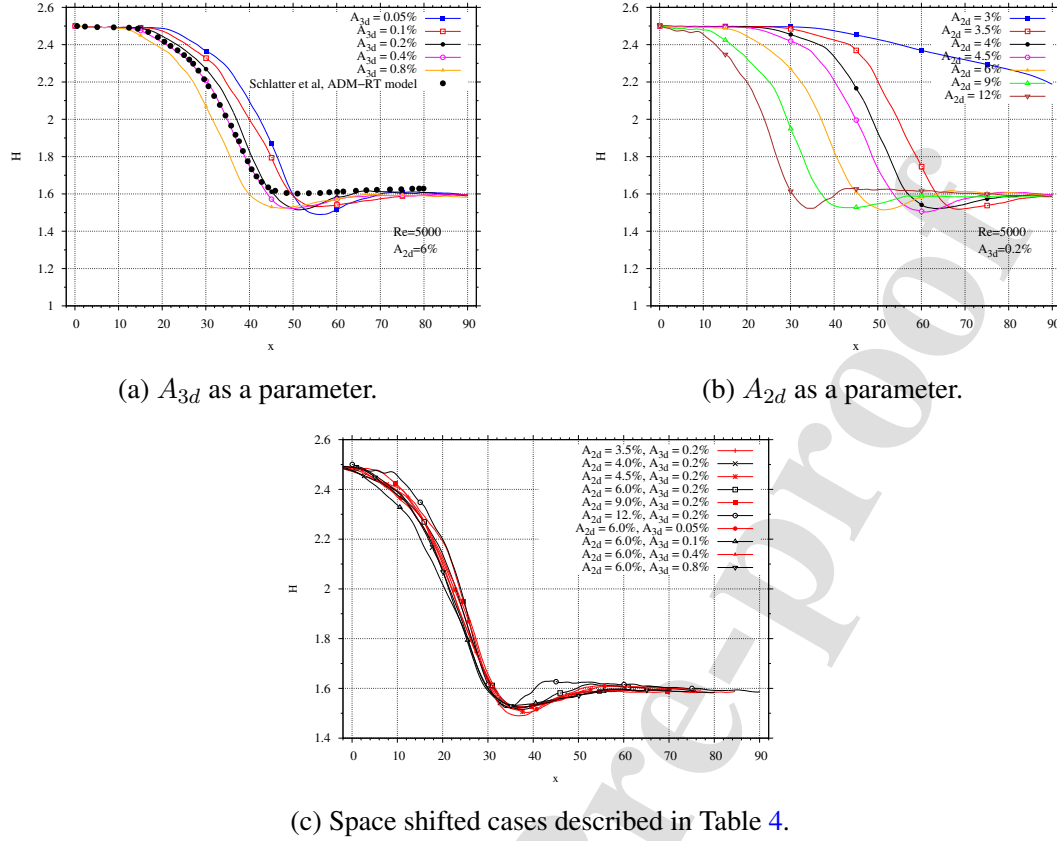
(a) A_{3d} as a parameter.

(b) A_{2d} as a parameter.

(c) Space shifted cases described in Table 4.

Figure 11: Space development of H with the amplitude as a parameter (Re = 5000). Reference data (Schlatter, 2005) in black dots in Figure 11a.

3.2 Comparison between two spatial transitions triggered by very different amplitude of perturbations

In the previous section we compared different transitional scenarios to show both: the weak dependence of the shape of the spatial evolution of integral quantities and the strong dependence of the location of the transitional departure, on the values of the amplitude of perturbations. In this section, an accurate comparison between two cases that yield transitions in locations separated by approximately 50 channel half-heights is carried out. The amplitude of perturbation for both cases are respectively A_{2d} = 6%, A_{3d} = 0.2% (case A) and A_{2d} = 3%, A_{3d} = 0.2% (case B). In Table 5 the parameters of each simulation are described. The domain for case B is significantly larger than that employed in the previous section to capture the transition. Both simulations were run for 500000 time steps and the statistics were taken during the last 100000 time steps.

Case A			Case B		
$L_x \times L_y \times L_z$	$n_x \times n_y \times n_z$	Δt	$L_x \times L_y \times L_z$	$n_x \times n_y \times n_z$	Δt
$100 \times 2 \times 3$	$2001 \times 65 \times 64$	0.001	$180 \times 2 \times 3$	$3601 \times 65 \times 64$	0.001

Table 5: Simulations' parameters for cases A and B.

3.2.1 Friction Reynolds number

As in the previous section, we shift results to match the Re_τ peak' location and this shift is used to compare other quantities in this section (here, case A is shifted 50 channel half-heights to the right). Figure 12 compares Re_τ for cases A and B after the shift. A qualitatively similar behavior of this parameter is found downstream $x \approx 70$. This reinforces the idea that the amplitude of the perturbations has a relatively small influence on the spatial evolution of this integral parameter in the transitional zone.

Also, six streamwise locations are remarked in this figure to serve as a reference for comparison purposes. These positions exemplify locations downstream the onset of the *spike* stage ($x \approx 70$): x_1 and x_2 in the super-late stage, x_3 in the peak transitional zone, x_4 in the post-transitional zone, x_5 in the final state of the post-transitional zone, and x_6 in the turbulent zone.
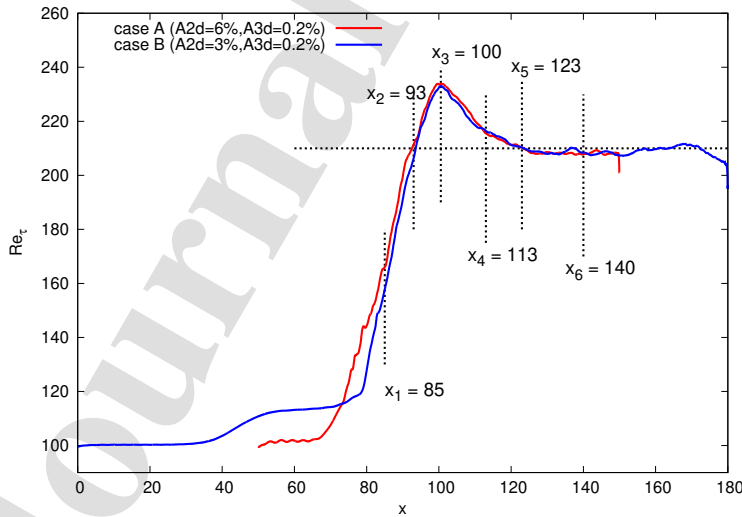
Figure 12: Re_τ vs. streamwise coordinate. Case A shifted and case B.

3.2.2 Vortex structures

We show in Figure 13 the vortex structures for case A (left, non shifted) and case B (right). These vortices are visualized using the λ_2 vortex visualization technique (Chakraborty et al., 2005; Sengupta et al., 2019). Figure 13.a shows the spanwise perturbation (TS waves) for both cases, where a higher size of the structures is found for case A (see the color of the isosurfaces for $\lambda_2 = -0.01$). The zone where these waves dominate is $0 \lesssim x \lesssim 10$ and $0 \lesssim x \lesssim 20$ for case A and B, respectively. These perturbations are periodic and increase their intensity with the streamwise direction defining the well known quasi-linear growth region where the friction Reynolds number is practically constant (see Figure 12). In figure 13.b the late stage is presented for both cases ($10 \lesssim x \lesssim 20$ and $20 \lesssim x \lesssim 70$ for cases A and B, respectively). In this region, a characteristic Λ vortex is generated due to the interaction between the TS waves and oblique waves, and the friction Reynoldsnumber increases moderately (see figure 12). At the end of this region, a *hairpin* vortex is generated as it is shown at $x \approx 24$ and $x \approx 70$ for the case A and B, respectively. This is the onset of the *spike* stage or super-late stage. From there, the *ring* vortices govern (Lu and Liu, 2012) and the friction factor increases rapidly. Moreover, the interaction between both walls can be recognized considering the vortex population at the center of the channel (see Figure 13.c). In this zone it can be observed that case A shows a denser population of coherent structures than case B but this fact is not reflected as a difference in the evolution of the friction Reynolds number. Finally, we can distinguish four zones in Figure 13.d (please consider case B, on the right, for the coordinate description) or figure 12: the final state of the super-late stage ($90 \lesssim x \lesssim 100$), the peak transitional zone ($x \approx 100$), the post-transitional zone ($100 \lesssim x \lesssim 130$) and the fully turbulent zone ($x \gtrsim 130$). In this region, both cases display a qualitatively and quantitative similar vortex structure and friction Reynolds number. This shows that both transitions are essentially equivalent downstream $x \approx 90$ (for Case B).
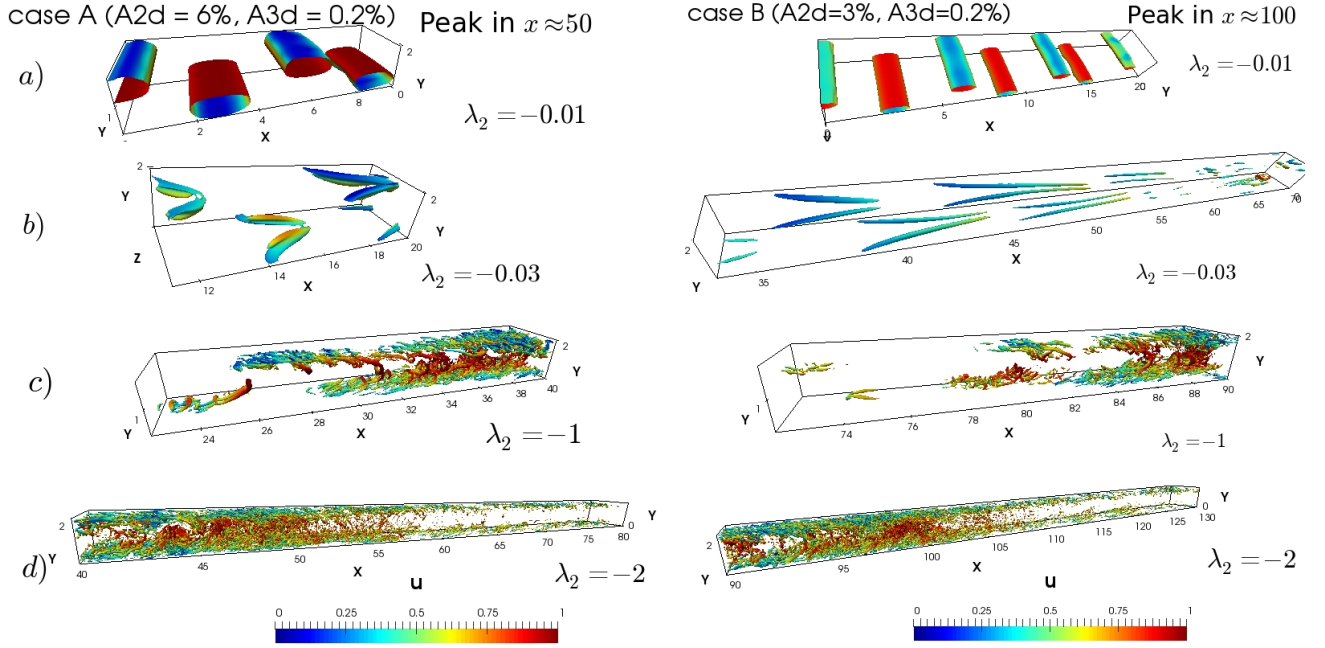
Figure 13: Vortices structures along the streamwise direction at $t = 460$ for case A (left) and case B (right), respectively. Isosurfaces of λ_2 colored with the streamwise velocity.

Other important parameter in the transitional phenomenon is the location of its onset. We can qualitatively relate this location with the head of the *hairpin* vortex (*ring* vortex), where high velocity fluctuations are generated (note figure 13.c right at $x \approx 70$). These fluctuations are shown in figure 14, where the streamwise and wall-normal velocity fluctuations at $z = 1.5$, $y = 0.01$ and $t = 460$ are presented for both cases (case A shifted). Near the channel inlet, fluctuations are characterized by the TS wave packet (figure 14a), which has a constant amplitude for a short length and then starts to decrease its amplitude (e.g. downstream $x \approx 40$ for case B) because the eigenvalue of the TS wave is stable for the simulated Reynolds number ($Re < 5772$ (Orszag, 1971)). Near $x \approx 70$ the *Spatio-Temporal Wave Front* (STWF) takes place to trigger the transitional process (Sengupta et al., 2020, 2018, 2006; Sengupta and Bhaumik, 2011). The STWF is generated by the interaction between the TS wave and the pair of oblique waves. In the literature, this stage is known as the *spike* stage due to the appearance of a high positive streamwise velocity fluctuation (Schlatter et al., 2004) (this will be discussed in section 3.3). After this stage, the wall-normal velocity fluctuation increases significantly too (see figure 14b). Thus, we can also define the location of the onset of the transition analyzing

the behavior of the streamwise and wall-normal velocity fluctuations yielded by the second sweep-ejection mechanism. Therefore, we can locate the onset of transition for cases A and B to be approximately at $x \approx 20$ and $x \approx 70$, respectively; which coincides approximately with the location where the first ring vortex appears.
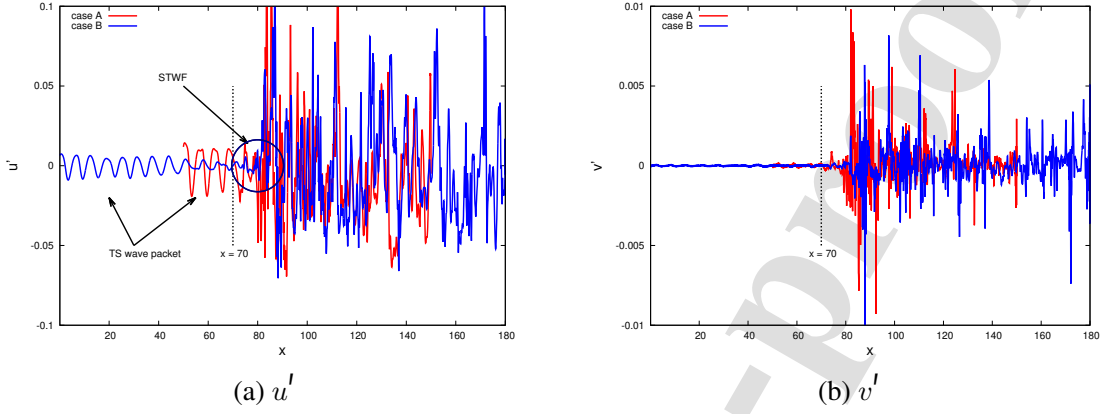

(a) u' (b) v'

Figure 14: Streamwise and wall-normal velocity fluctuations for cases A (red) and B (blue) as a function of streamwise direction at $z = 1.5$, $y = 0.01$ and $t = 460$.

3.2.3 First order parameters

Figure 15 shows the dimensionless streamwise velocity (time and spanwise averaged) in the developing region for both cases under consideration (downstream the late stage). Both cases seems to be qualitatively equal comparing this quantity. A more detailed look is shown in figure 16, where the velocity profiles are compared at the six streamwise positions remarked in Figure 12 (note that each streamwise velocity is normalized using its centerline velocity $< u_c >$). Overall, the velocity profiles are comparable in shape and magnitude along the transition. There are relatively small differences upstream the peak zone (x_1, x_2 and x_3) that can be explained considering that the larger population of vortex structures present in case A respect to case B (see figure 13.c) yields a relatively flatter profile.
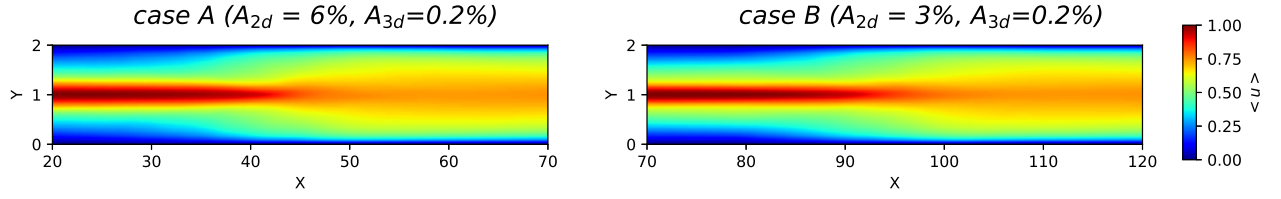
Figure 15: $< u >$ around the peak zone. Case A left and case B right.

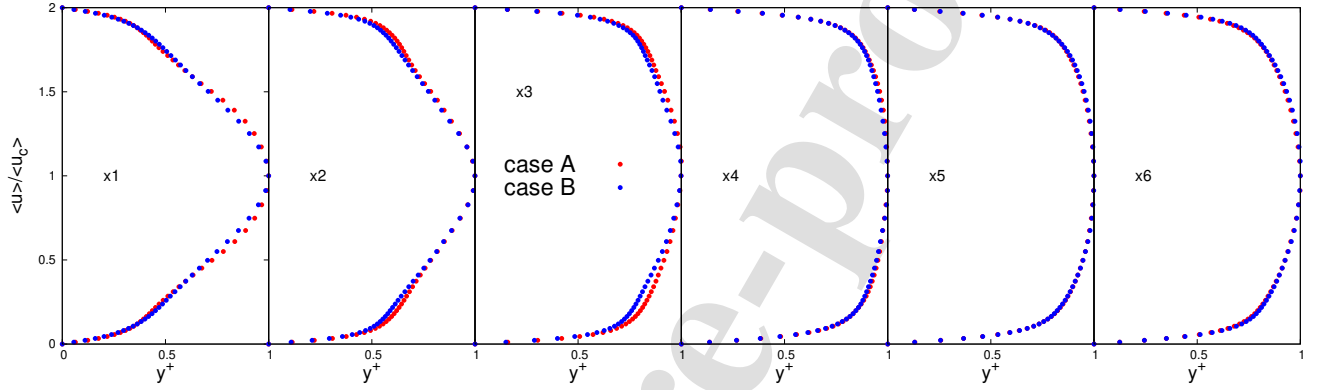Figure 16: $< u > / < u_c >$ at the six selected streamwise positions. ● case A, ● case B.

The fact that Λ vortices evolve faster for case A than case B (see figure 13.b) can also be appreciated in figure 17, where the shape factor is compared for both cases. For $x < 70$, case B displays a slower space development than case A, being its late stage longer than that corresponding to the other case. Downstream $x \approx 90$ the shape factor does not show significant differences between both cases.
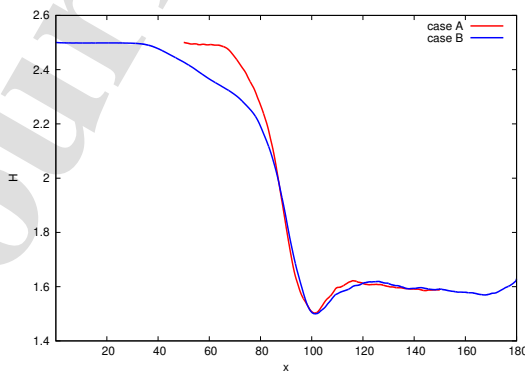

Figure 17: Shape factor for cases A (shifted) and B.

3.2.4 Second order parameters

Figure 18 shows the diagonal components of the Reynolds stresses, the TKE and turbulent shear stress upstream and downstream of the peak friction Reynolds number's position. Note that quantities have been averaged in time and z-coordinate.

Observing the figure it is clear that upstream $x \approx 40$ and $x \approx 90$ for case A (non shifted) and case B, respectively, the TKE is dominated by the contribution of $< u'u' >$. After this stage, the other two diagonal components of the stresses become significant but the main contribution to the TKE is still due to the streamwise component (see for instance Antonia et al. (2009) in turbulent channel flow).

Comparing cases A and B, it can be observed that the spatial distribution and the intensity of $< u'u' >$, and therefore TKE, are significantly different upstream the peak transitional zone but for the other two diagonal components of the Reynolds stresses are not. This reinforces the idea that the wall-normal and spanwise components need to grow to interact with the streamwise fluctuations to trigger the transitional process. The turbulent shear stress ($- < u'v' >$ shown in the last cartoon of the figure), has a qualitatively similar magnitude and space development for both cases. This fact is relevant to turbulence models that intend to capture the transition employing this quantity to define the turbulent viscosity.
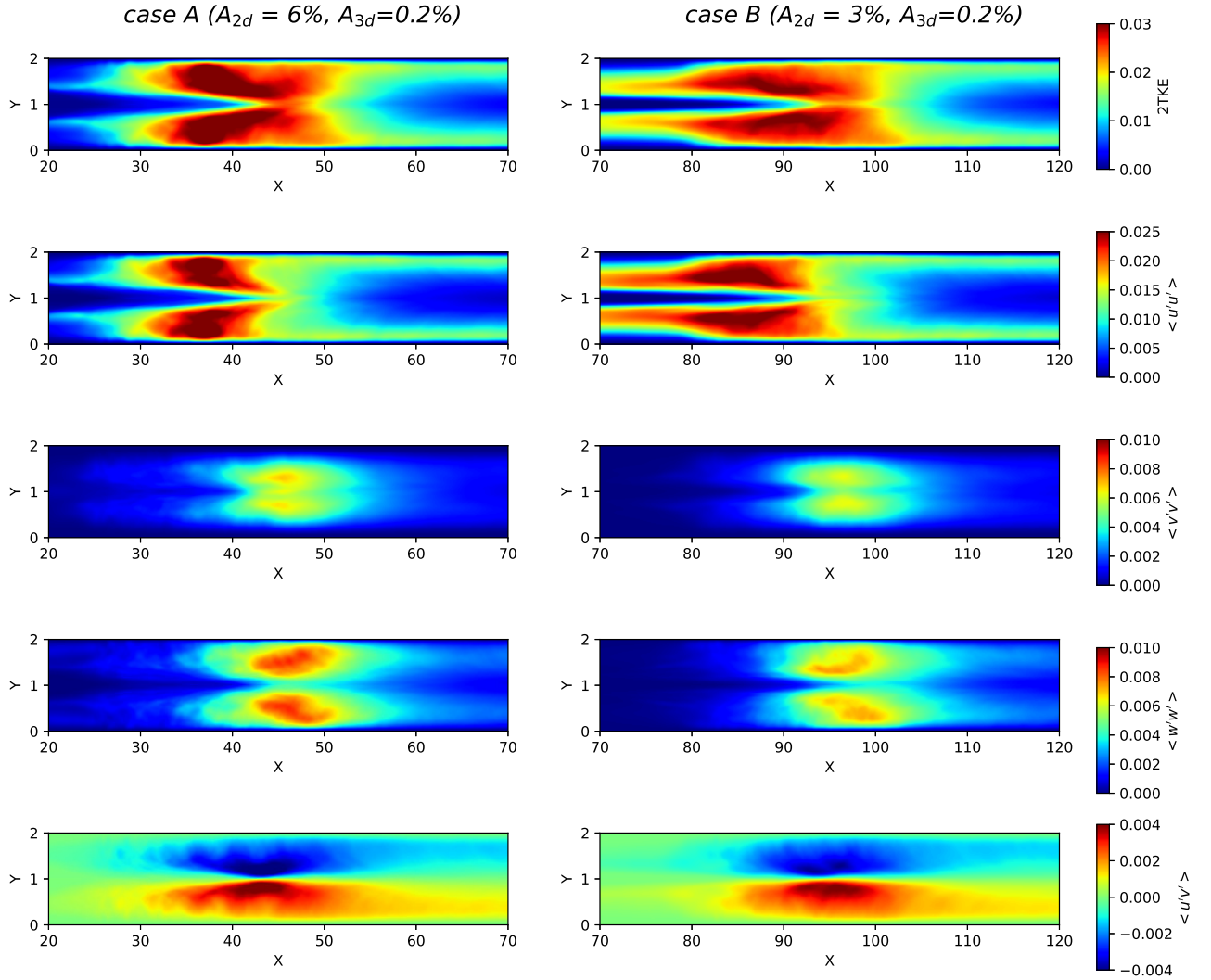
Figure 18: 2TKE and Reynolds stresses in outer units. Case A left and case B right.

Results discussed in figure 18 can be complemented considering figure 19, where the evolution of the TKE, Reynolds normal stresses and the turbulent shear stress is shown as a function of streamwise direction (quantities are now averaged also in the wall-normal direction, $<>_{wn}$, and case A is shifted). All these components evolve from the inlet value to the fully turbulent one passing through a peak of over production that is four or five times larger than their fully developed turbulent values. The cross-section averaged streamwise turbulent fluctuating velocity ($< u'u' >_{wn}$) develops first in space peaking approximately 10 channel half-heights upstream of the peak of the other diagonal components. These two, together with $- < u'v' >_{wn}$, depend

on the interaction between the oblique wave and the saturated 2D wave (secondary instability) and therefore develop later in space. We can see this effect considering case B, where the onset of spanwise and wall-normal turbulent fluctuating velocities is located 50 channel half-heights apart from the onset of the streamwise turbulent fluctuating velocity.

More in detail and for the lowest values of A_{2d} (case B), the TKE presents three zones upstream the peak location of Re_τ: a quasi-linear stage (e.g. $0 \lesssim x \lesssim 20$), where the TS waves interact with the 3D waves to destabilize the flow; the late stage (e.g. $20 \lesssim x \lesssim 70$), where the Λ vortices are present (Zang and Krist, 1989; Guo et al., 2010; Borodulin et al., 2002b); and the super-late stage or *spike* stage ($70 \lesssim x \lesssim 100$), (Schlatter et al., 2004), where the *ring* vortices are present. Analyzing case A and based on Figures 13, 18 and 19 we can observe that increasing A_{2d}, the quasi-linear stage and the late stage become shorter as the TS wave reaches its saturated state in a shorter distance from the inlet than the other case ((Schmid and Henningson, 2001; Bayly and Orszag, 1988)). Moreover, in the first state of the super-late stage ($70 \lesssim x \lesssim 90$), integral quantities present differences between both cases showing the influence of the amplitude of the TS wave in this zone. Downstream of the peak zone ($x \approx 100$), where there is no presence of coherent vortices (see figure 13), there are no significant differences between both cases. This shows that the mechanism that governs the post-transitional zone and the turbulent zone is essentially equivalent in them.
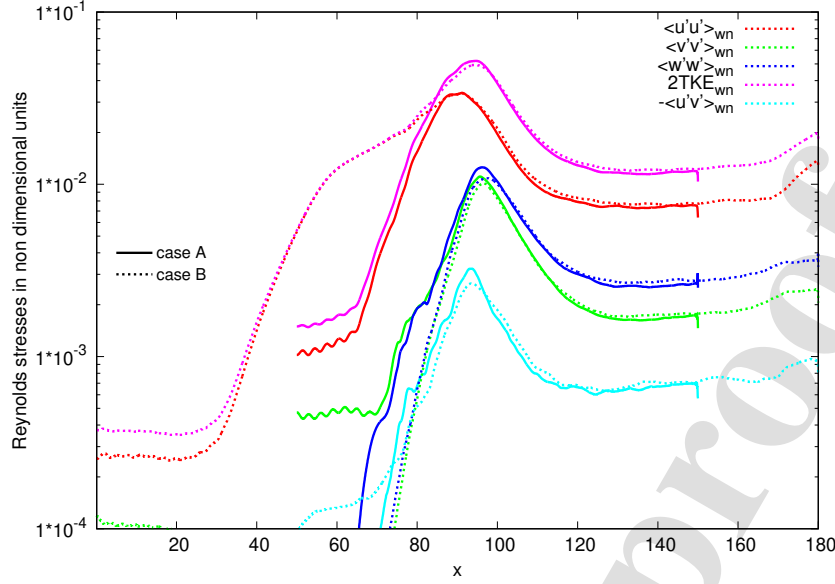
Figure 19: TKE, Reynolds normal stresses and turbulent shear stress in inner units (spanwise, wall-normal and time averaged). —case A, - - - -case B. —$2TKE_m$, —$< u'u' >_{wn}$, —$< v'v' >_{wn}$, —$< w'w' >_{wn}$, —$- < u'v' >_{wn}$.

To continue with the analysis, wall-normal profiles of Reynolds normal stresses and turbulent shear stress are shown in figure 20 at the six streamwise positions indicated in figure 12 (case B shifted). Additionally, fully developed values of these quantities computed by different sources are shown in the same figure for comparison purposes.

First, it is noted that upstream the peak position of the friction Reynolds number ($x < x_3$), quantities are greater than the corresponding fully developed values. This is due to the existence of large coherent structures that populate this zone (see figure 13). For example, at x_1, the presence of a *ring* vortex near the centerline (see figure 13.c) yields relatively high values of the Reynolds stresses ($< u'^+ u'^+ >$, $< v'^+ v'^+ >$, $< w'^+ w'^+ >$ and $- < u'^+ v'^+ >$). At x_2, the presence of a large coherent structure that mixes the flow with the highest possible intensity is located near the centerline. This coherent structure is identified in the peak of $< u'^+ u'^+ >$, $< v'^+ v'^+ >$, $< w'^+ w'^+ >$ and $- < u'^+ v'^+ >$. Downstream the peak position (x_3), good agreement is found between reference data and present results near the wall ($y^+ < 20$). In the logarithmic region, profiles still evolve to reach a fully developed turbulent regime at x_5. These two facts suggest that the decrease of the friction Reynolds number in this region (see figure 12) can be associated with the variations of the second order parameters in the logarithmic layer. Comparing the

space evolution of the second order parameters of both cases, we observe that both transitions are essentially similar downstream x_2 showing that the influence of the perturbations is limited to the first state of the super-late stage ($70 \lessapprox x \lessapprox 90$ for case B).
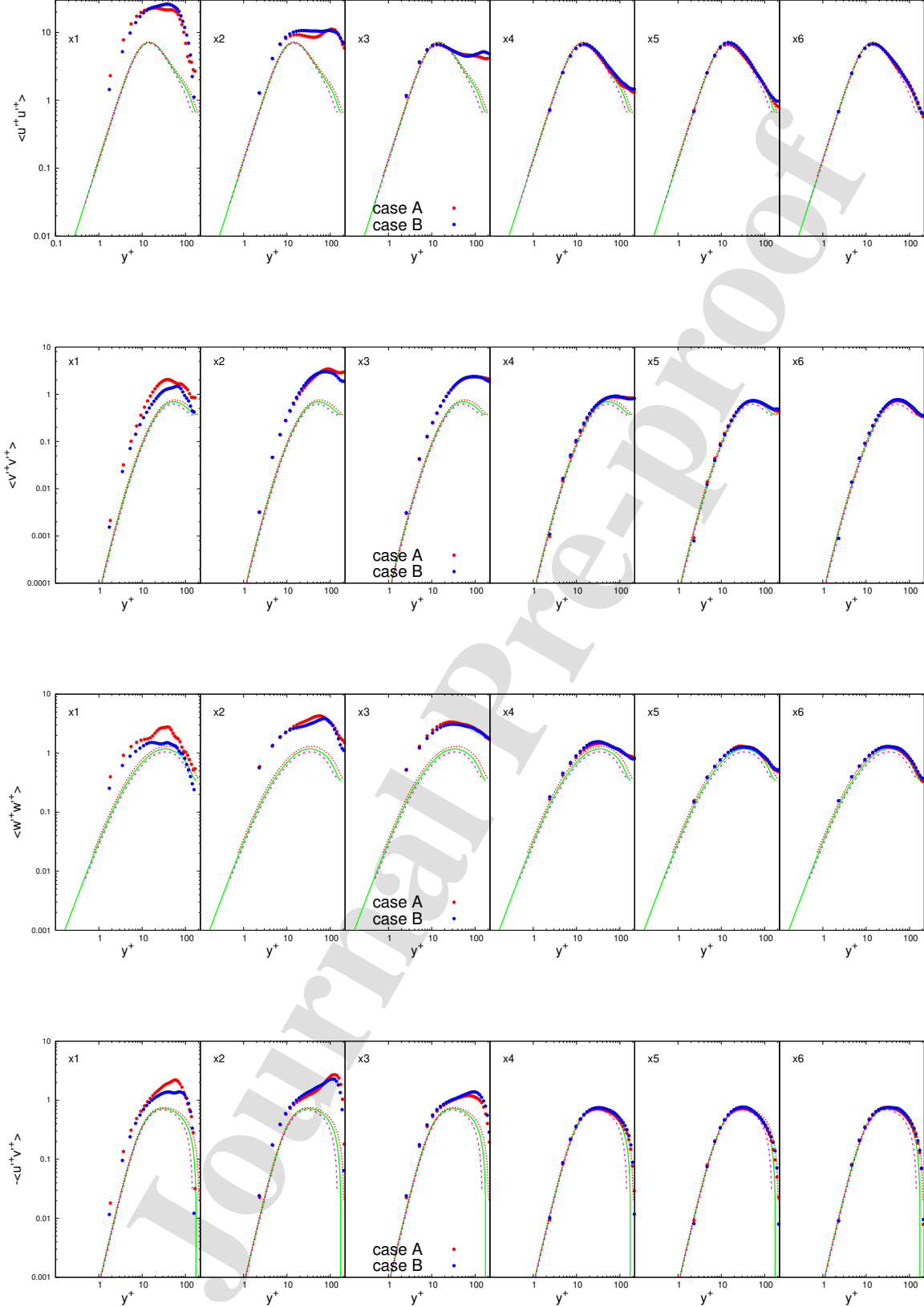
Figure 20: Profiles of the Reynolds normal stresses ($< u'^+ u'^+ >$, $< v'^+ v'^+ >$, $< w'^+ w'^+ >$) and turbulent shear stress ($- < u'^+ v'^+ >$) at six streamwise positions for $Re = 5000$. ● case A, ● case B. Reference data calculated in periodic turbulent channel flow: —Moser et al. (1999) at $Re_\tau \approx 180$, - - - -Flageul (2015) at $Re_\tau \approx 150$ and - - - -Incompact3d code (IC3D) at $Re_\tau \approx 210$.

3.2.5 Budget of the streamwise turbulent fluctuating velocity

In this subsection we will discuss the larger component of the TKE, the streamwise turbulent fluctuating velocity. For that purpose, a study of the budget of $< u'u' >$ is carried out for both cases considering the balance:

$$
\begin{aligned}
< u > \frac{\partial < u'u' >}{\partial x} &= -2 < u'u' > \frac{\partial < u >}{\partial x} - 2 < u'v' > \frac{\partial < u >}{\partial y} \quad ...(P) \\
&\quad - \frac{\partial < u'u'u' >}{\partial x} - \frac{\partial < u'u'v' >}{\partial y} \quad ...(TD) \\
&\quad - 2 < u'\frac{\partial p'}{\partial x} > \quad ...(V-PGCorr.) \\
&\quad \frac{1}{Re}(\frac{\partial^2}{\partial x \partial x} < u'u' > + \frac{\partial^2}{\partial y \partial y} < u'u' >) \quad ...(VD) \\
&\quad - \frac{2}{Re}(< \frac{\partial u'}{\partial x}\frac{\partial u'}{\partial x} > - < \frac{\partial u'}{\partial y}\frac{\partial u'}{\partial y} > - < \frac{\partial u'}{\partial z}\frac{\partial u'}{\partial z} >) \quad ...(Diss.)
\end{aligned}
\tag{19}
$$

where the l.h.s. of equation 19 is the convective term (Conv.), and the terms on the r.h.s. are respectively: Production (P), Turbulent Diffusion (TD), Velocity-Pressure Gradient correlation (V-PG Corr.), Viscous Diffusion (VD) and Dissipation (Diss.).

In figure 21 the six components of the budget are shown in nondimensional units (averaged in time, spanwise and wall-normal direction). Considering the magnitude, this budget is dominated by the production, dissipation and velocity-pressure gradient terms. This was also found by He and Seddighi (2013) in the turbulent transient channel flow, but different from that, here the velocity-pressure gradient correlation term has a greater intensity in the peak zone than that corresponding to the dissipation term. This can be explained considering that we are simulating a K-type transition at a moderate Reynolds number while the other study considers a *bypass* transition, where the TS wave is bypassed. Additionally, in comparison with the temporal transition, where the periodic boundary condition in the streamwise direction avoids any influence of the convective term in the budget, here, this term places a role in the transitional zone as the time derivative does in the temporal transition.

Another relevant aspect is that the onset of the V-PG Corr. term is at $x \approx 70$ (downstream

the onset of Production and Dissipation terms). This quantity is a source for the wall-normal and spanwise turbulent fluctuating velocities (see figure 19 and 18). Thus, the departure of this quantity can also be employed as the onset of the transition.

The comparison between both cases shows that case B presents a larger growth of the Production and Dissipation terms in the late stage ($20 \lesssim x \lesssim 70$) than those calculated for Case A. Also, in the first state of the super-late stage ($70 \lesssim x \lesssim 90$) both cases present differences in the Production, Velocity-pressure gradient correlation and Convection terms. Downstream x_2 (the last state of the super late stage) there are no significant differences between both cases showing, again, that both transitions are essentially similar.
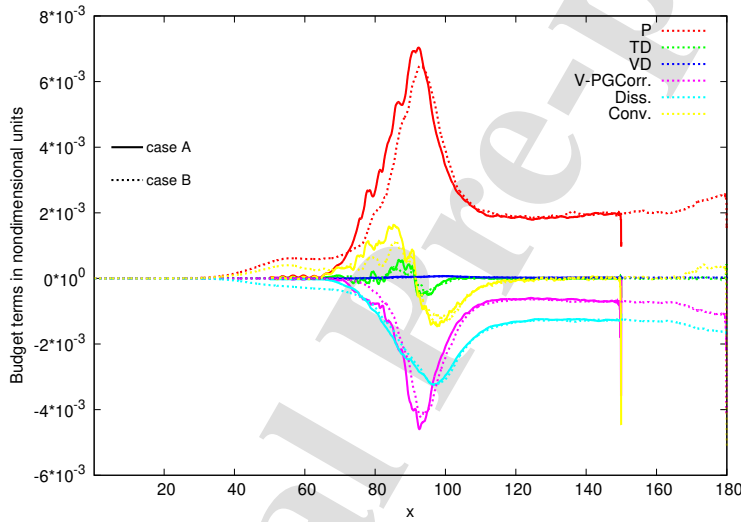

Figure 21: Space evolution of the cross-section averaged components of the streamwise turbulent fluctuating velocity budget. ——case A, - - - - -case B. ——Production, ——Turbulent diffusion, ——Viscous diffusion, ——Velocity-pressure gradient correlation, ——Dissipation and ——Convection.

With DNS results we can compute the space evolution of the profiles of each term of the $< u'^+ u'^+ >$ budget at the six different streamwise positions indicated in figure 12. Figure 22 shows this evolution together with fully developed reference values.

With respect to the transitional process, at x_1 and x_2, the presence of large coherent structures yields higher intensity of the components near the wall and in the centerline region, than those found at fully developed values. Specifically, at x_2, the Production, velocity-pressure gradient correlation, turbulent-diffusion and convection terms present a peak near the centerline as a

consequence of the large population of coherent structures (see figure 13). Downstream x_3, the convection term is negligible and the components of the budget have approximately reached their fully developed stages. This suggests that the mechanism that governs this budget in this region is related to the self-sustained turbulence mechanism.

Considering a comparison between both cases, despite the fact that at x_1 the components of the budget differ, downstream x_2, where the population of vortices have grown across the height of the channel, both cases display a strong similarity showing that this budget is no longer influenced by the TS wave amplitude imposed at the inlet.
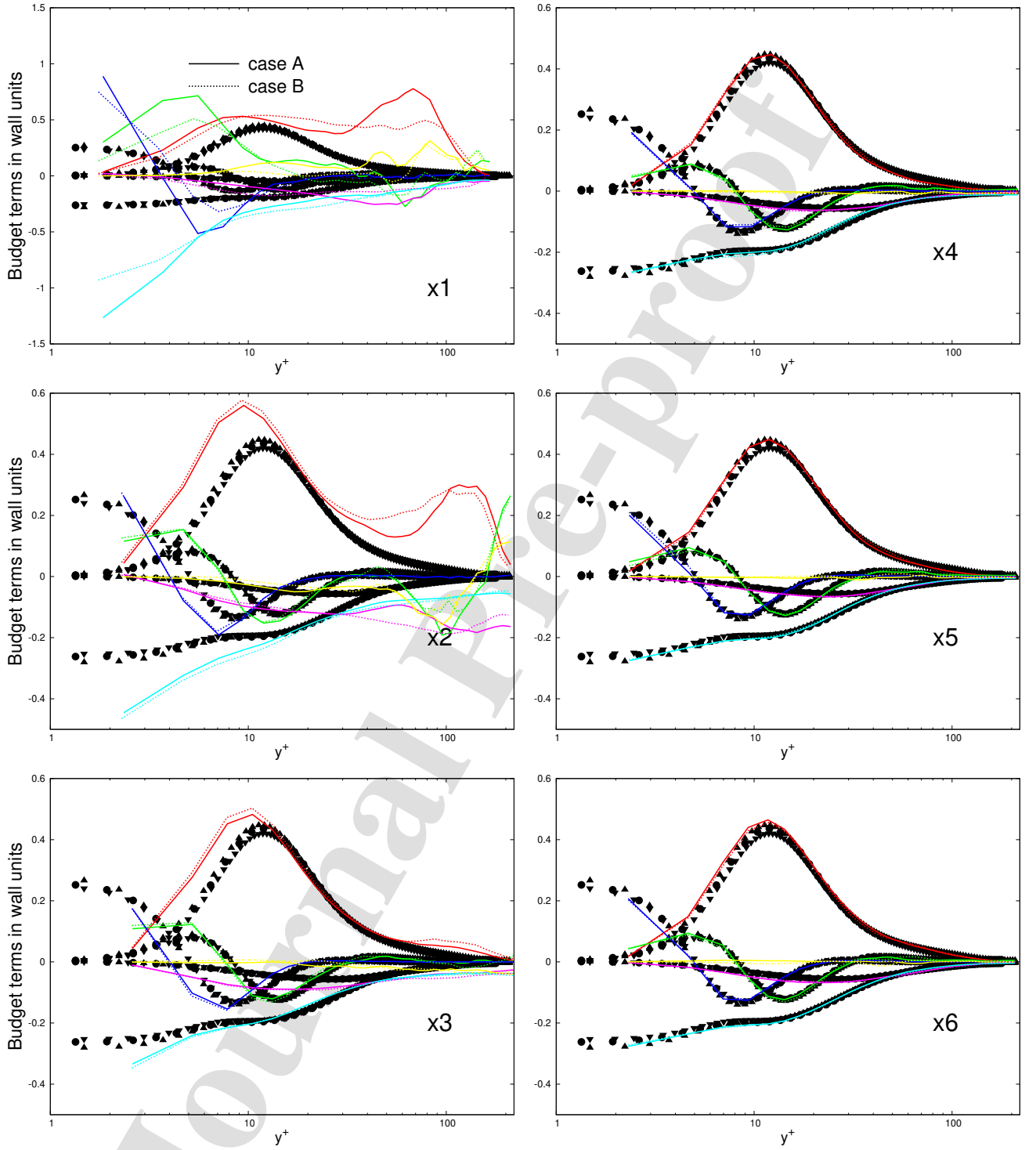
Figure 22: Profiles of the streamwise turbulent fluctuating velocity budget at six streamwise position for $Re = 5000$. ——case A, $\cdots\cdots$ case B. ——Production (P), ——Turbulent diffusion (TD), ——Viscous diffusion (VD), ——Correlation between Velocity and Pressure Gradient (V-PGCorr), ——Dissipation (Diss.) and ——Convection (Conv.). Reference data calculated in periodic turbulent channel flow: ● calculated by Moser et al. (1999) at $Re_\tau \approx 180$, ▲ calculated using Incompact3d code at $Re_\tau \approx 210$, ▼ calculated by Flageul (2015) at $Re_\tau \approx 150$.

3.3 Peak in the transitional zone

In this section we will discuss aspects related to the formation of a peak in the spatial evolution of Re_τ using the mechanism described in section 1. That is the increase of the Reynolds shear stress is due to the multilevel sweep and ejection mechanisms that are present in the evolution of the *hairpin* vortex structures (Liu and Lu, 2012; Liu et al., 2014). Quantitatively, both mechanisms can be analyzed by the theory of quadrant analysis (Shaw et al., 1983; Adrian, 2007; Chen and Liu, 2011), where the sweep and ejection mechanisms can be quantified by $(u' < 0, v' > 0)$ and $(u' < 0, v' > 0)$, respectively. Both mechanisms mix the flow increasing the Reynolds shear stress (Chen and Liu, 2011). Moreover, in the evolution of the coherent *hairpin* vortices, *spikes* are generated by the first sweep and second sweep of the ring vortices, which generate high shear layer areas. Then, it is clear that after the *spike*, the Reynolds shear stress increases significantly its absolute value. Using this information, the high shear layer areas can be identified employing the analysis of streamwise velocity fluctuations (u') together with the spanwise vorticity (Lu and Liu, 2012).

In figure 23 we show the mean and instantaneous values ($t = 460$) of Re_τ as a function of streamwise coordinate (case A of the previous section). There are five zones with different characteristics (see figure 13): the quasi-linear zone ($0 \lesssim x \lesssim 10$), where the TS wave are predominant (see the oscillations of the instantaneous Re_τ); the late stage ($10 \lesssim x \lesssim 20$), where the Λ vortex are predominant and a decrease of the amplitude of the TS wave is present at the final of this stage (see the instantaneous Re_τ in figure 23 at $x \approx 20$); the super-late stage or *spike* stage ($20 \lesssim x \lesssim 50$), where the *ring* vortex is present; the peak transitional zone ($x \approx 50$); the zone right after the peak location ($50 \lesssim x \lesssim 70$), the post-transitional zone; and finally, the turbulent zone ($70 \lesssim x \lesssim 100$). We first consider the zone upstream the peak transitional zone.
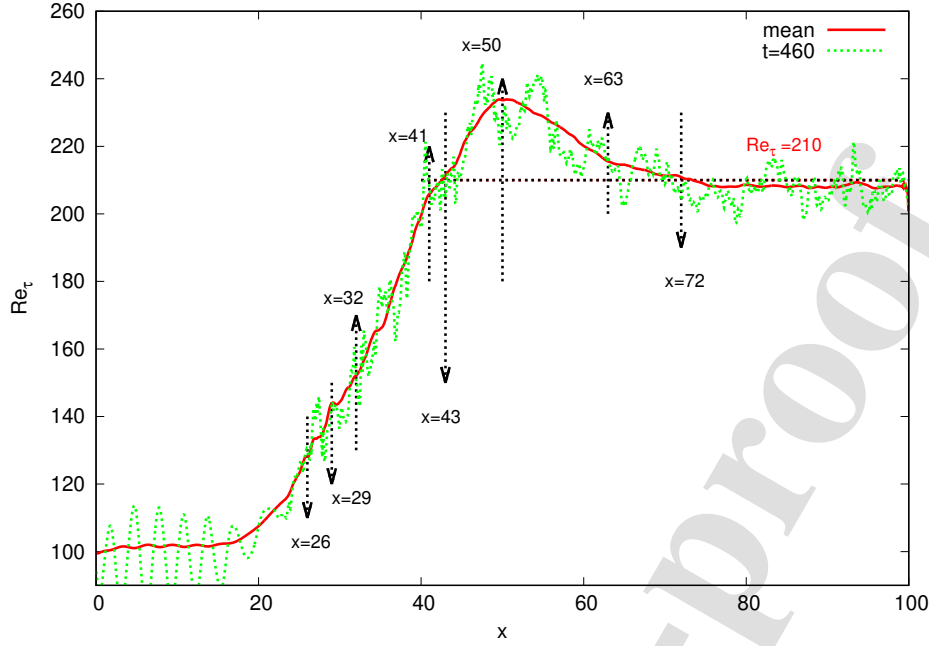
Figure 23: Time-average and instantaneous Re_τ at $t = 460$.

In figure 24, the streamwise velocity fluctuation u' and the absolute value of the spanwise vorticity $|\omega_z|$ are shown for different x positions upstream the peak transitional zone ($x \approx 50$). At $x = 26$ we already observe relatively high values of velocity fluctuations near walls and relatively high shear layer areas ($\omega_z \approx \frac{\partial u}{\partial y}$). These areas correspond to the legs of the hairpin vortices (see case A in figure 13.b at $x \approx 26$), which yield the first sweep-ejection mechanism. At $x = 29$ and $x = 32$, these relatively high values appear also at the bulk of the channel. This is because the *hairpin* vortex moves away from the walls (see figure 13.c) and generates the second sweep-ejection mechanism. Downstream $x = 32$, the physical phenomenon is more complex because the coherent *hairpin* vortices spread across the entire height of the channel interacting between them. This mechanism increases the high shear layer areas in the entire channel cross-section as can be seen at $x = 41$. This zone is not completely chaotic and a sort of symmetry can be identified in the spanwise vorticity and velocity fluctuations around $z \approx 1.5$ (note the walls and centerline zones). This symmetry indicates that coherent vortices are present and bring high energy from the centerline to the walls increasing the shear layer (see spanwise vorticity at $x = 41$). Along with this evolution, the increase of the shear layer translates as an increase of the friction Reynolds number.

This analysis is complemented with figure 25, in which the instantaneous streamwise velocity at $t = 460$ as a function of z is shown at different streamwise positions and $y = 0.01$ (bottom wall). At $x = 26$ the legs of the hairpin vortex increase/decrease the velocity due to the first sweep-ejection mechanism (e.g. note the peak at $z \approx 0.75$). At $x = 29$, two *spikes* can be observed at $z \approx 1.1$ and $z \approx 1.8$ respectively. These *spikes* are generated by the second sweep of a *ring* vortex (see also u' in figure 24 in $x = 29$ at bottom wall), and generate high shear layer areas increasing the Reynolds shear stress value (Chen and Liu, 2011; Liu and Lu, 2012; Liu et al., 2014; Liu and Lu, 2014). At $x = 32$, the population of *ring* vortices is growing which generate quasi-streamwise vortices and more intense *spikes* than those found upstream. Downstream $x = 32$, the coherent structures expands in z direction with a complex vortex interaction, which generate high intensity fluctuation zones on the entire channel cross-section (see figure 24 and 25 in $x = 41$). This is exemplified in Figure 25 with relative high values of the instantaneous streamwise velocity at the walls at $x = 41$. At this location there is still some symmetry around $z = 1.5$.
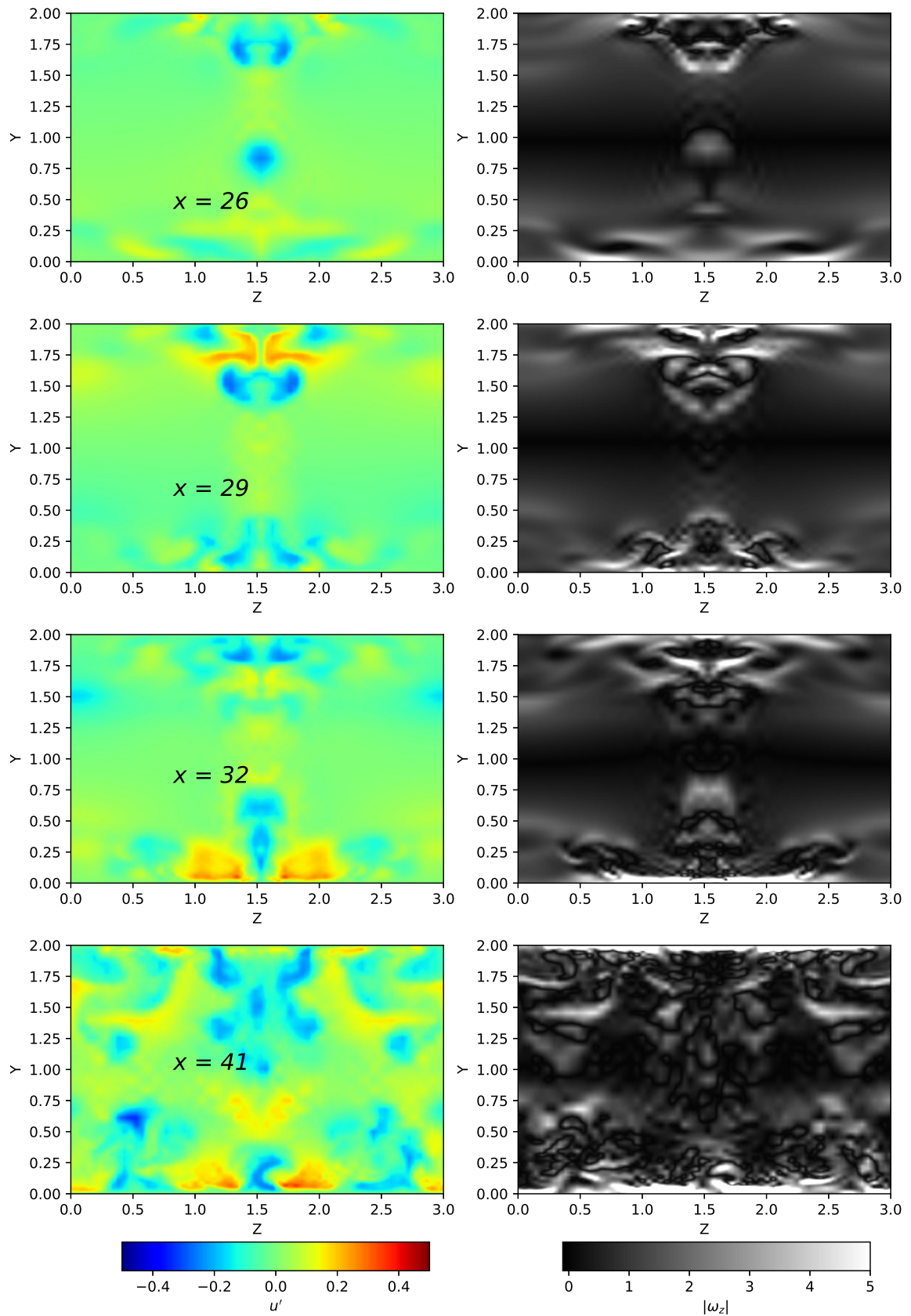
Figure 24: Cross-section view of the streamwise velocity fluctuation (left) and absolute span-wise vorticity (right) along the transition at $t = 460$.
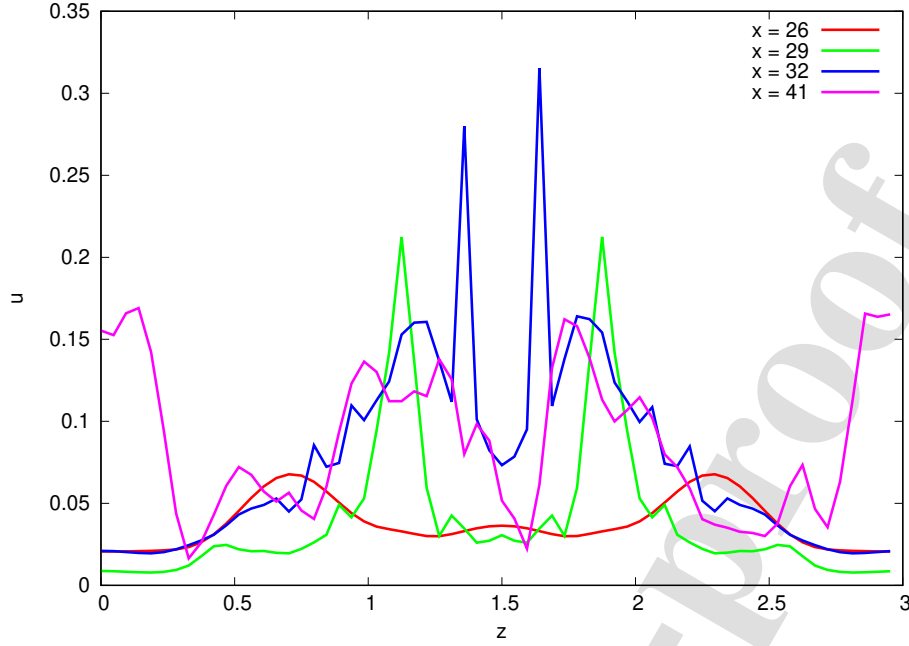
Figure 25: Streamwise velocity as a function of spanwise direction for different x positions at $t = 460$ and $y = 0.01$.

To continue the analysis downstream $x = 41$ (last state of the super-late stage), the key is to consider the coherent *ring* vortices (see figure 13.c), that yield, through the second sweep mechanism (Chen and Liu, 2011; Guo et al., 2010), the generation of high positive *spikes* and high shear layer areas. Nevertheless, when these *hairpin* vortices lose their coherence, they lose their capacity to bring energy from the centerline (high energy zone) to the walls. We will then analyze the coherence of vortex structures near the peak zone. In figure 26, at $x = 43$, high intensity zones are shown near the centerline and near the wall, which indicates the presence of large structures (ring vortex, see figure 13.c). In this position (super-late stage) there is still a certain symmetry about $z = 1.5$. These coherent structures yields a near-centerline peak in the profile of $< u'^{+} u'^{+} >$ (see figures 20 and 22 at x_2 position). At $x = 50$, Figure 26 still displays high intensity zones of the quantities in the entire section but the symmetry about $z = 1.5$ is practically lost and the *ring* vortices do not longer occupy the channel bulk. Continuing, at $x = 63$ and $x = 72$, there is no evidence of the presence of the coherent *hairpin* vortices. The high intensity zones and structures are being dissipated in the bulk of the channel and are located only near walls generating small scales flow structures (see case A of figure 13.d in these

two positions at the bulk). In this process the friction Reynolds number is decaying to its fully turbulent value and the flow is mainly governed by the self-sustained turbulent mechanism.
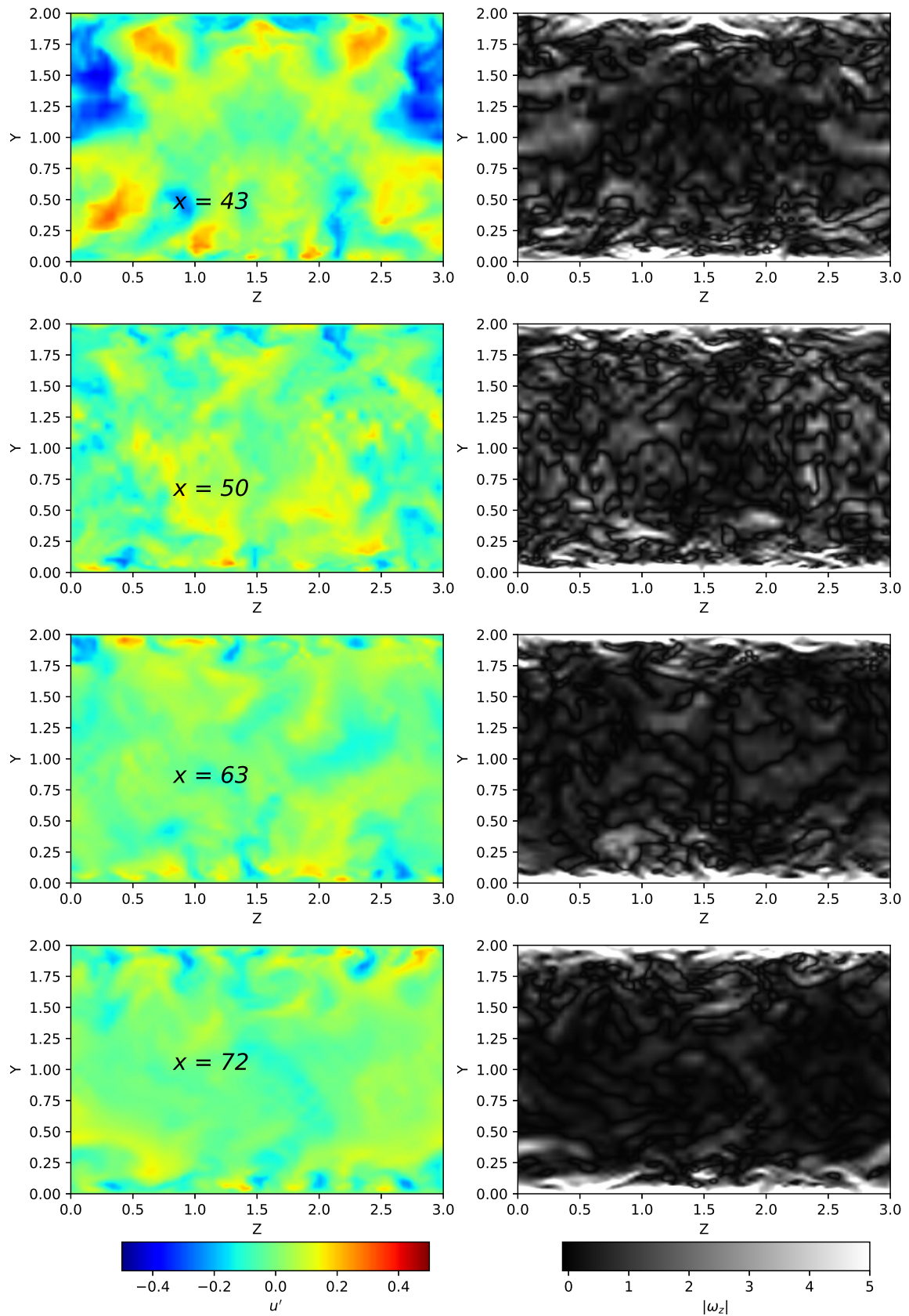
Figure 26: Cross-section view of the streamwise velocity fluctuation (left) and absolute spanwise vorticity (right) along the transition at $t = 460$.

4   SUMMARY AND CONCLUSIONS

A methodology to model the spatial transition in a plane channel flow employing the open source code Incompact3D was described in this study. Simulations are characterized by the imposition of a Poiseuille flow perturbed by the most unstable modes of the Orr-Sommerfeld and Squire eigenvalue problem as an inlet BC. In most of the cases simulated the complete transition was achieved in domains of 90 channel half-heights in length in the streamwise direction.

First and for $Re = 5000$, eleven simulations with different amplitudes of the TS and 3D waves were studied to show two important aspects: the shape of Re_τ in the transition (growth, peak and decay to a fully developed value) is roughly independent on the amplitude of perturbations and the location of the peak is, on the contrary, strongly dependent on it.

Second, we considered two cases with different TS wave amplitudes ($A_{2d} = 6\%$ and $A_{2d} = 3\%$ respectively) that present friction Reynolds number peaks separated by approximately 50 channel half-height diameters.

The study of the streamwise evolution of integral quantities shows that both cases present a quasi-linear growth at the inlet region, where the TS waves dominate and the integral quantities are approximately constant. A late stage follows, with the formation of Λ vortices and a moderate growth of Re_τ and shape factor. At the end of this region, a *hairpin* vortex is generated, which is the onset of the *spike* stage (super-late stage). In this stage, the STWF mechanism acts and the velocity-pressure gradient correlation term of the budget of $< u'u' >$ increases significantly its value giving place to the increase of the spanwise and wall-normal turbulent fluctuating velocities. At this stage, approximately all quantities increase their values at a relatively high speed and, therefore, the onset of the present K-type transition can be defined with the onset of the *spike* stage. Downstream the peak transitional zone, vortex structures lose their coherence and integral quantities decay to reach a fully developed turbulent state.

The study of the $< u'u' >$ budget along the transition shows that the most important terms, considering the magnitude, are the production, dissipation and velocity-pressure gradient correlations being the last one more important than the dissipation in the near peak zone.

We computed profiles of different turbulent quantities at six streamwise positions down-

stream the onset of the *spike* stage to find that upstream the peak position (x_2 in the last state of the super-late stage), the Reynolds stresses and all the streamwise turbulent fluctuating velocity budget terms (except the viscous diffusion term), present a peak near the centerline as a result of the presence of large coherent structures in this region. Downstream the peak transitional zone, these quantities are in good agreement with the reference data in the near-wall region while, in the logarithmic region, profiles are still evolving to reach a fully developed turbulent regime at x_5 (final state of the post-transitional zone). Also, the mechanism that governs the $< u'^+ u'^+ >$ budget downstream the peak location is related to the self-sustained turbulence mechanism.

Overall, we can observe that despite the fact that both cases need different distances to achieve the transition, the information imposed at the inlet through the perturbations is essentially lost downstream x_2 (the last state of the super-late stage). The influence of the TS wave in both cases is present in the quasi-linear stage, in the late stage and in the first state of the super-late stage. However, downstream x_2, we found a very similar evolution of both cases.

Finally, the spatial evolution of the friction Reynolds number was discussed employing streamwise velocity fluctuations and the spanwise vorticity as tools to explain the sweep-ejection mechanism. Upstream the friction Reynolds number peak zone we show that there is coherence in the vortex structures. This coherence allows bringing high energy from the centerline to the wall increasing the friction Reynolds number up to the peak transitional zone. After this zone, vortices near the centerline lose their coherence and dissipate, and the high shear layer areas are limited to the near-wall region. In this process we observe a decay of the friction Reynolds number to its fully developed value.

5 ACKNOWLEDGEMENTS

REFERENCES

Abraham J.P., Sparrow E., and Minkowycz W.J. Internal-flow nusselt numbers for the low-reynolds-number end of the laminar-to-turbulent transition regime. *International Journal of Heat and Mass Transfer*, 54:584–588, 2011.

Abraham J.P., Sparrow E.M., Tong J., and Bettenhausen D. Internal flows which transist from turbulent through intermittent to laminar. *International Journal of Thermal Sciences*, 49:256–263, 2010.

Adrian R.J. Hairpin vortex organization in wall turbulence. *Physics of Fluids.*, 19:1–16, 2007.

Adrian R.J., Meinhart C.D., and Tomkins C.D. Vortex organization in the outer region of a turbulent boundary layer. *Phys. Fluids*, 422:1–54, 2000.

Antonia R.A., Abe H., and Kawamura H. Analogy between velocity and scalar fields in a turbulent channel flow. *J. Fluid Mech.*, 628:241–268, 2009.

Avila K., Moxey D., de Lozar A., Avila M., Barkley D., and Hof B. The onset of turbulence in pipe flow. *Science*, 333:192–196, 2011.

Bayly B.J. and Orszag S.A. Instability mechanism in shear-flow transition. *Ann. Rev. Fluid Mech.*, 20:359–391, 1988.

Benhamou B. L.A. and Galanis N. Transition to turbulence: The case of a pipe in radial oscillations. *International Journal of Thermal Sciences*, 43:1141–1151, 2004.

Borodulin V.I., Gaponenko V.R., and Kachanov Y.S. Late-stage transitional boundary-layer structures. direct numerical simulations and experiment. *Theoret. Comput. Fluids Dynamics*, 15:317–337, 2002a.

Borodulin V.I., Kachanov Y.S., and Koptsev D.B. Experimental study of resonant interactions of instability waves in a self-similar boundary layer with an adverse pressure gradient: I. tuned resonances. *Journal of Turbulence*, 3(62):1–38, 2002b.

Buffat M., Le Penven L., Cadiou A., and Montagnier J. Dns of bypass transition in entrance channel flow induced by boundary layer interaction. *European Journal of Mechanics B/Fluids*, 43:1–13, 2014.

Chakraborty P., Balachandar S., and Adrian R.J. On the relationships between local vortex

identification schemes. *J. Fluid Mech.*, 535:189–214, 2005.

Chen L. and Liu C. Numerical study on mechanisms of second sweep and positive spikes in transitional flow on a flat plate. *Computers and Fluids*, 40:28–41, 2011.

Criminale W.O., Jackson T.L., Lasseigne D.G., and Joslin R.D. Perturbation dynamics in viscous channel flow. *J. Fluid Mech*, 239:55–77, 1997.

Flageul C. *Création de bases de données fines par simulation directe pour les effets de la turbulence sur les transferts thermiques pariétaux*. PhD Tesis, Université de Poitiers, France, 2015.

Gioia G. and Chakraborty P. Turbulent Friction in Rough Pipes and the Energy Spectrum of the Phenomenological Theory. *Physical Review Letters*, 96:044502, 2006.

Guo H., Borodulin V.I., Kachanov Y.S., Pan C., Wang J.J., Lian Q.X., and Wang S.F. Nature of sweep and ejection events in transitional and turbulent boundary layers. *Journal of Turbulens*, 11(34):1–51, 2010.

He S. and Seddighi M. Turbulence in transient channel flow. *J. Fluid Mech.*, 715:60–102, 2013.

Henningson D., Lundbladh A., and Johansson A. A mechanism for bypass transition from localized disturbances in wall-bounded shear flows. *Journal of Fluid Mechanics*, 250:169–207, 1993.

Herbert T. Secondary Instability of Boundary Layers. *Annual Review of Fluid Mechanics*, 20:487–526, 1988.

Juniper M.P. Modal stability theory. *Applied Mechanics Review*, 66:024804, 2014.

Klebanoff P., Tidstrom K., and Sargent L. The three-dimensional nature of boundary-layer instability. *Journal of Fluid Mechanics*, 12:1–34, 1962.

Kleiser L. and Zang A. Numerical simulation of transition in wall-bounded shear flows. *Annual Review of Fluid Mechanics*, 23:495–537, 1991.

Laizet S. and Lamballais E. High-order compact schemes for incompressible flows: A simple and efficient method with quasi-spectral accuracy. *J.C. Physics*, 228(16):5989–6015, 2009.

Laizet S., Lamballais E., and Vassilicos J.C. A numerical estrategy to combine high-order schemes, complex geometry and parallel computing for high resollution DNS of fractal gen-

erated turbulence. *Computers and Fluids*, 39(3):471–484, 2010.

Laizet S. and Li N. Incompact3d: A powerful tool to tackle turbulence problems with up to $O(10^5)$ computational cores. *Int. J. Numer. Meth. Fluids*, 67:1735–1757, 2011.

Lamballais E. Direct numerical simulation of a turbulent flow in a rotating channel with a sudden expansion. *J. Fluid Mech.*, 745:92–131, 2014.

Lemoult G., Gumowski K., Aider J., and Wesfreid J. Turbulent spots in channel flow: an experimental study. *Eur. Phys. J. E.*, 37:25, 2014.

Liu C. and Chen L. Study of mechanism of ring-like vortex formation in late flow transition. In *48th AIAA Aerospace sciences meeting including the new horizons forum and aeroespace exposition*, pages 1–21. Orlando, Florida, 2010.

Liu C. and Liu Z. Multigrid mapping and box relaxation for simulation of the whole process of flow transition in 3D boundary layers. *Journal of Computational Physics*, 119(2):325–341, 1995.

Liu C. and Lu P. Dns study on physics of late boundary layer transition. In *50th AIAA Aerospace sciences meeting including the new horizons forum and aeroespace exposition*, pages 1–30. Nashville, Tennessee, 2012.

Liu C. and Lu P. Dns stydy on turbulence structure in a boundary layer. In *50nd Aerospace Sciences Meeting*, pages 1–79. Maryland, 2014.

Liu C., Yan Y., and Lu P. Physics of turbulence generation and sustenance in a boundary layer. *Computers & Fluids*, 102:353–384, 2014.

Lorenzini M. M.G.L. and Salvigni S. Laminar, transitional and turbulent friction factors for gas flows in smooth and rough microtubes. *International Journal of Thermal Sciences.*, 49:248–255, 2010.

Lu P. and Liu C. Dns study on mechanism of small length scale generation in late boundary layer transition. *Physica D*, 241:11–24, 2012.

Lu P., Thapa M., and Liu C. Surface friction and boundary layer thickening in transitional flow. *Advances in Modeling of Fluid Dynamics*, pages 1–14, 2012a.

Lu P., Yan Y., and Liu C. Numerical study on mechanism of multiple rings formation. In

50th AIAA Aerospace sciences meeting including the new horizons forum and aeroespace exposition, pages 1–13. Nashville, Tennessee, 2012b.

Lundbladh A., Schmid P., Berlin S., and Henningson D. Simulations of bypass transition for spatially evolving disturb. *AGARD-CP-551*, 18:1–13, 1994.

Luo J. and Hui L. Influence of small imperfections on the stability of plane poiseuille flow: A theoretical model and direct numerical simulation. *Physics of Fluids*, 16:8, 2004.

Machaca Abregu W.I. *Esquemas compactos de alto orden para el estudio de la transferencia de calor en régimen de transición*. Tesis de Maestría en Ingeniería, Instituto Balseiro, Universidad Nacional de Cuyo, 2015.

Machaca Abregu W.I. and Teruel F.E. *Estudio de las estructuras de vorticidad en la transición espacial laminar-turbulenta en canales angostos*. ENIEF 2016, Códoba, Argentina, 2016.

Minkowycz W.J., Abraham J.P., and Sparrow E.M. Numerical simulation of laminar breakdown and subsequent intermittent and turbulent flow in parallel-plate channels: Effects of inlet velocity profile and turbulence intensity. *International Journal of Heat and Mass Transfer*, 52:4040–4046, 2009.

Moser R.D., Kim J., and Mansour N.N. Direct numerical simulation of turbulent channel flow up to $Re_\tau = 590$. *Phys. Fluids*, 11(4):943–945, 1999.

Orszag S.A. Accurate solutionof the Orr-Sommerfeld stability equation. *J. Fluid Mech.*, 50(4):698–703, 1971.

Quadrio M., Frohnapfel B., and Hasegawa Y. Does the choice of the forcing term affect flow statistics in DNS of turbulent channel flow. *European Journal of Mechanics B/Fluids*, 55:286–293, 2016.

Saiki E., Biringen S., Danabasoglu G., and Streett C. Spatial simulation of secondary instability in plane channel flow: comparison of k- and h-type disturbances. *Journal of Fluid Mechanics*, 253:485–507, 1993.

Sano M. and Tamai K. A universal transition to turbulence in channel flow. *Nature Physics*, 12:249–254, 2016.

Schlatter P. *Large-Eddy simulation of transition and turbulence in wall-bounded shear flow.*

PhD tesis, Swiss Federal Institute of Technology, Zurich, 2005.

Schlatter P., Stolz S., and Kleiser L. Les of transitional flows using the approximate deconvolution model. *International Journal of Heat and Fluid Flow*, 25:549–558, 2004.

Schlatter P., Stolz S., and Kleiser L. Large-eddy simulation of spatial transition in plane channel flow. *Journal of Turbulence*, 7:33, 2006.

Schmid P.J. and Henningson D.S. Stability and Transition in Shear Flows. In *Applied Mathematical Sciences*, volume 142. Springer, 2001.

Seki D. and Matsubara M. Experimental investigation of relaminarizing and transitional channel flows. *Physics of fluids*, 24:124102:1–23, 2012.

Sengupta A., Suman V.K., Sengupta T.K., and Bhaumik S. An enstrophy-based linear and nonlinear receptivity theory. *Phyics of Fluids*, 30:054106:1–19, 2018.

Sengupta A., Sundaram P., and Sengupta T.K. Nonmodal nonlinear route of transition to two-dimensional turbulence. *Physical Review Research 2*, 012033:1–6, 2020.

Sengupta T.K. and Bhaumik S. Onset of turbulence from the receptivity stage of fluid flows. *Physical Review Letters*, 107:154501:1–5, 2011.

Sengupta T.K., Rao A.K., and Venkatasubbaiah K. Spatiotemporal growing wave fronts in spatially stable boundary layers. *Physical Review Letters*, 96:224504:1–4, 2006.

Sengupta T.K., Sharma P.K., Sengupta A., and Suman V.K. Tracking disturbances in transitional and turbulent flows: Coherent structures. *Physics of Fluids*, 31:124106, 2019.

Shaw R.H., Tavangar J., and Ward D.P. Structure of reynolds stress in a canopy layer. *J. Clim. Appl. Meteorol.*, 22:1922–1931, 1983.

Silin N., Masson V., and García G. Convection in a rectangular channel with a flow of water in laminar-turbulent transition with high heat fluxes. *Experimental Heat Transfer*, 40:125–130, 2010.

Teruel F. and Rizwan-uddin. An innovative research reactor design. *Nuclear Engineering and Design*, 239:395–407, 2009.

Theodorsen T. Mechanism of turbulence. In *Proc. Second Midwestern Conj. of Fluid Mechanics*, pages 1–19. Ohio State University, Columbus, Ohio, 1952.

Trefethen N. *Spectral Methods in Matlab*. SIAM, Philadelphia, U.S.A., 2000.

Vinuesa R., Noorani A., Lozano-Durán A., Khoury G.K., Schlatter P., Fischer P.F., and Nagib H.M. Aspect ratio effects in turbulent duct flows studied through direct numerical simulation. *Journal of Turbulence*, 15(10):677–706, 2014.

Wang Y., Al-Dujaly H., Yan Y., and Zhao N. Physics of multiple level hairpin vortex structures in turbulence. *Physics, Mechanics and Astronomy, Science China*, 59(2):1–11, 2016.

Zang T.A. and Krist S.E. Numerical experiments on stability and transition in plane channel flow. *Theoret. Comput. Fluid Dynamics*, 1:41–64, 1989.

Zhou J., Adrian R., and Balachantar S. Mechanisms for generating coherent packets of hairpin vortices in channel flow. *Journal of Fluid Mechanics*, 387:353–396, 1999.

Zhou J., Adrian R.J., and Balachantar S. Autogeneration of near-wall vortical structures in channel flow. *Physics of Fluids.*, 8(1):288–290, 1996.

Highlights

- The friction Reynolds number in the transition region is roughly independent on the amplitude of the perturbations at the inlet.
- The location of the departure of the transition process is strongly dependent on the amplitudes of the perturbations.
- Two spatial transitions triggered by very different amplitude of perturbations were compared.
- Five stages were identified in both transitional scenarios: quasi-linear stage, late stage, spike stage, peak transitional zone, post-transitional zone and fully turbulent zone.
- The influence of the amplitude of the perturbations is limited to the first state of the super-late stage.
- The peak transitional zone in the friction Reynolds number can be explained considering the coherent vortices packet found across the height of the channel in the super-late stage of the transition.

Credit Author Statement

- **W. I. Machaca Abregu:** Conceptualization, Methodology, Software, Validation, Formal Analisis, Investigation, Visualization, Writing.
- **Enzo A. Dari:** Methodology, Software, Resources., Supervision.
- **Federico E. Teruel:** Conceptualization, Methodology, Resources, Formal Analisis, Investigation, Writing, Supervision.

Declaration of interests

☒ The authors declare that they have no known competing financial interests or personal relationships that could have appeared to influence the work reported in this paper.

☐ The authors declare the following financial interests/personal relationships which may be considered as potential competing interests: